The Astrophysical Journal, 572:762–785, 2002 June 20


# FOUR YEARS OF MONITORING BLAZAR PKS 2155−304 WITH *BeppoSAX*: PROBING THE DYNAMICS OF THE JET

Y. H. Zhang,[1] A. Treves,[1] A. Celotti,[2] L. Chiappetti,[3] G. Fossati,[4] G. Ghisellini,[5] L. Maraschi,[6] E. Pian,[7] G. Tagliaferri,[5] and F. Tavecchio[6]

*Received 2001 November 20; accepted 2002 February 20*

## ABSTRACT

PKS 2155−304 is one of the brightest blazars in the X-ray band. It was repeatedly monitored with *BeppoSAX* during three long campaigns of about 2 days each in November of 1996, 1997, and 1999. The source underwent different states of intensity and was clearly variable with successive flares detected. This paper presents temporal and spectral analysis to study the X-ray variability trends for a blazar. The variability shows larger amplitude and shorter timescale at higher energies. The power spectral densities have steep power-law slopes of ∼2–3, indicating shot-noise variability. Structure function analysis reveals the existence of a "typical" timescale characteristic of the half-duration of the flares. From the cross-correlation analysis we find that the values of soft lags, i.e., delays of soft (0.1–1.5 keV) photons with respect to hard (3.5–10 keV) ones, differ from flare to flare, ranging from a few hundred seconds to about 1 hr. There is a suggestion that the flares with shorter duration show smaller soft lags. The soft lags are also energy-dependent, with longer lags of lower energy emission with respect to the emission in the 4–10 keV range. The time-resolved X-ray spectral fits with a curved model show that peak energies of the synchrotron component are located in the very soft X-ray range or even below the *BeppoSAX* lower energy limit, 0.1 keV. A correlation between peak energies and fluxes is marginal. Spectral evolution during some flares shows clockwise loops in the spectral index–flux plane, confirming the soft lags indicated by the cross-correlation analysis. Two flares, however, show evidence that spectral evolution follows opposite tracks in the soft- and hard-energy bands, respectively. The rich phenomenology is interpreted in the context of a model in which relativistic electrons are accelerated through internal shocks taking place in the jets. The most important parameter turns out to be the initial time interval between the two shells ejected from the central engine to produce the flare, which may determine the structure of the shock and, in turn, the physical quantities of the emitting region used to reproduce the observed trends of the X-ray variability.

*Subject headings:* BL Lacertae objects: general — BL Lacertae objects: individual (PKS 2155−304) — galaxies: active — methods: data analysis — X-rays: galaxies

## 1. INTRODUCTION

The most remarkable property that discriminates blazars from other active galactic nuclei (AGNs) is that they are strongly and rapidly variable from radio to gamma rays on different timescales. From the point of view of the observations, there has been clear progress made in the last decade. EGRET, on board the *Compton Gamma-Ray Observatory*, has detected about 60 blazars that are (GeV) gamma-ray–emitting sources (Hartman et al. 1999), and gamma rays from a few nearby sources have been detected up to the TeV energies with ground-based Cerenkov telescopes. Gamma-ray observations have revealed the remarkable feature that the overall spectral energy distribution (SED) of a blazar shows two distinct components in the $\nu$-$\nu F_\nu$ representation, typically characterized by their peak energies. The first (low-energy) component peaks from millimeter to the X-ray, while the second (high-energy) one peaks at GeV–TeV energies. In such a picture, the blazar family could be unified according to the SEDs that are parameterized by the bolometric luminosity (see, e.g., Fossati et al. 1998). The emission is believed to be produced by relativistic electrons tangled with the magnetic field in a relativistic jet through two processes. Synchrotron radiation is responsible for the low-energy component, while inverse Compton upscattering by the same population of electrons produces the high-energy component (see, e.g., Ghisellini et al. 1998). The jet is supposed to be oriented close to the line of sight. Superluminal motions observed with VLBI suggest that the bulk Lorentz factor of the jets is on the order of $\Gamma \sim 10$ (see, e.g., Vermeulen & Cohen 1994). Relativistic beaming is thus a marked feature of blazars.

Constructing the overall SED and determining the relationships in different energy bands can, in principle, constrain the physical parameters and emitting mechanisms taking place in blazars. Moreover, the temporal evolution of both the SED and the interband relationships enables us to explore the dynamics and structure of the jets, which ultimately give clues on the physical properties of the central massive black hole system. However, because of limitations of the observations, the earlier studies of blazars were

[1] Dipartimento di Scienze, Università dell'Insubria, via Valleggio 11, I-22100 Como, Italy; youhong.zhang@uninsubria.it.
[2] International School for Advanced Studies, SISSA/ISAS, via Beirut 2-4, I-34014 Trieste, Italy.
[3] Istituto di Fisica Cosmica G. Occhialini, IFCTR/CNR, via Bassini 15, I-20133 Milano, Italy.
[4] Center for Astrophysics and Space Science, University of California at San Diego, 9500 Gilman Drive, La Jolla, CA 92093-0424.
[5] Osservatorio Astronomico di Brera, via Bianchi 46, I-22055 Merate, Italy.
[6] Osservatorio Astronomico di Brera, via Brera 28, I-20121 Milano, Italy.
[7] Osservatorio Astronomico di Trieste, via G.B. Tiepolo 11, I-34131 Trieste, Italy.

mainly based on the "snapshot" SEDs (most of them are not simultaneous). Short time coverage and undersampling of the data have prevented detailed studies of the evolution of the SED and of interband correlations. Relatively higher quality data from recent monitoring of a few nearby TeV sources, especially in the X-ray and TeV energies, have allowed us to establish two important properties in these sources: correlated X-ray/TeV variability (see, e.g., Maraschi et al. 1999) and energy-dependent time lags in the X-ray (see, e.g., Zhang et al. 1999). These results have provided important clues on the acceleration and cooling mechanism of relativistic electrons.

Up to now, the X-ray energy band is still the best in which to perform the detailed studies of variability in TeV-emitting sources since the most pronounced variations are expected in such a band, which represents the highest energy tail of the synchrotron component. Studies of the variability expected in the highest energy end of the Compton component, i.e., TeV energies, are still limited at present because of undersampling. Mrk 421 and Mrk 501 have been intensively monitored with *BeppoSAX*. The remarkable findings are the detection of significant upshifts of synchrotron peak energies in Mrk 501 (Pian et al. 1998; Tavecchio et al. 2001) and high-energy photons lagging behind the low-energy ones in Mrk 421 (Fossati et al. 2000a; Zhang 2000).

PKS 2155−304 is a nearby TeV-emitting blazar ($z = 0.116$; Falomo, Pesce, & Treves 1993) with the synchrotron emission peaking in the UV–soft X-ray range. Because of the brightness, PKS 2155−304 is one of the best targets to monitor across the whole electromagnetic spectrum. It has been repeatedly observed at optical (Zhang & Xie 1996 and references therein; Xie et al. 2001), UV (Pian et al. 1997; Marshall 2001), X-ray (Treves et al. 1989; Sembay et al. 1993), gamma-ray (Vestrand, Stacy, & Sreekumar 1995), and TeV energies (Chadwick et al. 1999). These observations have demonstrated complex multiwavelength variability in PKS 2155−304 (Edelson et al. 1995; Urry et al. 1997). Correlated variability in different X-ray bands and physical implications have been reported in Chiappetti et al. (1999), Zhang et al. (1999), Zhang (2000), Kataoka et al. (2000), and Edelson et al. (2001). Mrk 421 and Mrk 501 have exhibited similar phenomenology as well (Takahashi et al. 1996, 2000; Fossati et al. 2000a; Zhang 2000; Tanihata et al. 2001).

PKS 2155−304 was also monitored with *BeppoSAX* during three long campaigns (about 2 days each), allowing us to explore its variability properties in different brightness states. Therefore, these observations will provide us with direct information on the evolution of the underlying physical processes, which in turn can give some valuable clues on the dynamics and the structure of the jets. Temporal and spectral analyses of the 1996 and 1997 campaigns were presented in Giommi et al. (1998), Chiappetti et al. (1999), and Zhang et al. (1999). In this paper we perform temporal and spectral analysis for the third campaign, i.e., the 1999 data set. Since for a direct comparison, a homogeneous set of results is necessary, we reanalyze the 1996 and 1997 data sets, focusing on issues not handled in the papers cited above.

This paper is organized as follows: The observations are introduced in § 2. Section 3 presents the light curves followed by temporal analysis with various methods, including estimators of variability (amplitude and doubling timescale), variations of hardness ratios, power spectral density, structure function, and cross-correlation function. The time-resolved spectral analysis is conducted in § 4, where we emphasize the evolution of synchrotron peak energies and spectral indices. In § 5 we summarize and compare the most important results presented in this and other works, followed by a discussion of their implications to the dynamics and the structure of the jet. Our conclusions are derived in § 6.

## 2. OBSERVATIONS

For a detailed description of the Italian/Dutch *BeppoSAX* mission, we refer to Boella et al. (1997 and references therein). The co-aligned Narrow-Field Instruments on board *BeppoSAX* consist of one Low Energy Concentrator Spectrometer (LECS; 0.1–10 keV), three identical Medium Energy Concentrator Spectrometers (MECS; 1.5–10 keV), a High-Pressure Gas Scintillation Proportional Counter (4–120 keV), and a Phoswich Detector System (13–300 keV). Because of the limited statistics of other instruments, in this work only data from the LECS and MECS are considered to suite to our purpose of analysis. The MECS was composed at launch of three identical units. On 1997 May 6 a technical failure caused the switch-off of the unit MECS1. All observations after this date were performed with only two units (i.e., MECS2 and MECS3).

The journal of the observations is summarized in Table 1. The observing efficiency, defined as the ratio of net exposure to the observing time, is ∼0.2 and ∼0.5 for the LECS and MECS detector, respectively. These low efficiencies are mainly due to periodic interruptions caused by the Earth occultation of a low Earth orbit satellite (with period of ∼1.6 hr) and other reasons such as passages through South Atlantic Anomaly, a high-background region, etc. Moreover, the effective LECS exposure time is significantly shortened because LECS is exposed only during the part of the orbit in the Earth shadow cone to avoid light leakage in the LECS instrument.

Our analysis is based on the linearized, cleaned event files for the LECS and MECS experiments. The events from the

TABLE 1
JOURNAL OF OBSERVATIONS

| OBSERVING TIME (UTC) | DURATION (hr) | NET EXPOSURE | | ARCHIVE NUMBER |
|---|---|---|---|---|
| | | LECS (ks) | MECS (ks) | |
| 1996 Nov 20 00:15:58–1996 Nov 22 13:30:06..... | 51.2 | 36.29 | 106.9 | 50016001 |
| 1997 Nov 22 16:03:00–1997 Nov 24 01:35:12..... | 32.5 | 22.49 | 59.49 | 50160008 |
| 1999 Nov 4 04:27:27–1999 Nov 6 16:52:12..... | 60.4 | 46.12 | 104.0 | 50880001 |

two (1997 and 1999) or three (1996) units of MECS are merged together to improve the photon statistics. These event files, together with appropriate background event files, are produced at the *BeppoSAX* Science Data Center (SDC; v0.2, v1.1, and v2.0) and are available from the *BeppoSAX* SDC on-line archive.[8] The event files are further screened with a good time interval file (from SDC) to exclude events without attitude solution (i.e., for these events, it is impossible to convert detector to sky coordinates; see Fiore, Guainazzi, & Grandi 1999).

The photons of the source were accumulated from events within a circular region centered on the position of the point source, and the extraction radii are 8′ and 6′ for LECS and MECS, respectively, which are typical radii applied to the bright and soft sources, like PKS 2155−304 (see, e.g., Fiore et al. 1999), and ensure that more than 95% of the photons are collected at all energies. No background light curves were estimated and subtracted since the estimated background count rates are on the order of about 1% of the source count rates.

## 3. TEMPORAL ANALYSIS

### 3.1. *Light Curves and Hardness Ratio*

In Figures 1–3 the light curves in the 0.1–1.5 (LECS), 1.5–3.5, and 3.5–10 keV (MECS) bands and the hardness ratios between them are reported. Each light curve has been divided into several parts, coinciding with the single flares considered in our analysis. Each flare is numbered and separated by the dotted lines. During all three observation epochs, which refer to rather different X-ray emission states of PKS 2155−304, X-ray variability is clearly detected, showing recurrent flares and no quiescent state. In the fol-

[8] See http://www.asdc.asi.it/mmia/index.php?mission=saxnfi.

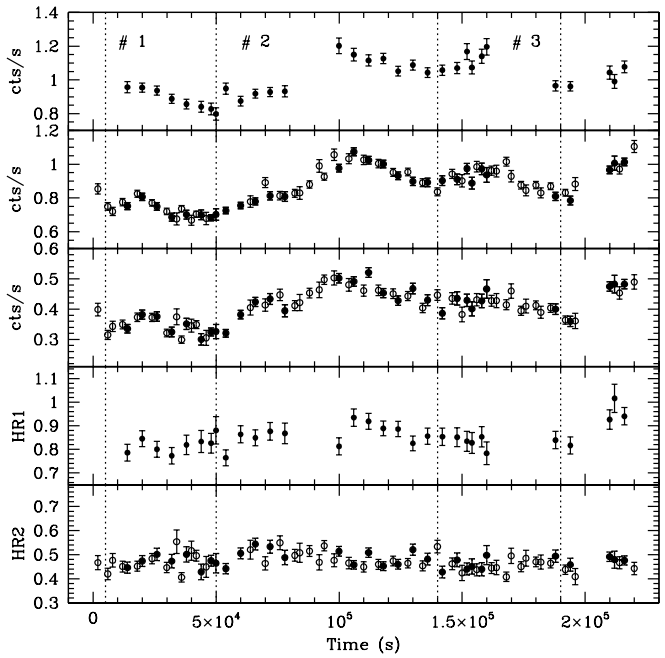


FIG. 1.—Light curves and hardness ratios of the 1996 November 20–22 observation. Data are rebinned over 2000 s. The reference time is 1996 November 20 (TJD = 10,407) 00:00:00 UT. *From top to bottom*: light curves in the 0.1–1.5, 1.5–3.5, and 3.5–10 keV bands and the hardness ratio between the 1.5–3.5 and 0.1–1.5 keV bands (HR1) and between the 3.5–10 and 1.5–3.5 keV bands (HR2). Note that the temporal coverage of the LECS is much more sparse than that of the MECS. The simultaneous LECS and MECS data points are indicated by filled symbols. The whole data set is divided into three parts that, in principle, contain single flares separated by the vertical dotted lines and numbered as flare 1, flare 2, and flare 3.

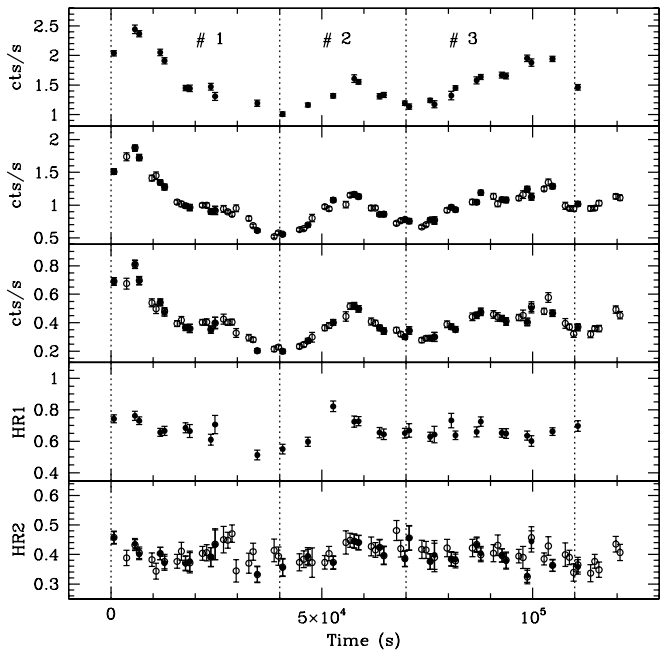


FIG. 2.—Light curves and hardness ratios of the 1997 November 22–24 observation. Data are rebinned over 1000 s. The reference time is 1997 November 22 (TJD = 10,774) 16:00:00 UT. The panels and symbols have the same meanings as those in Fig. 1. This data set is basically divided into three single flares numbered as flare 1, flare 2, and flare 3.

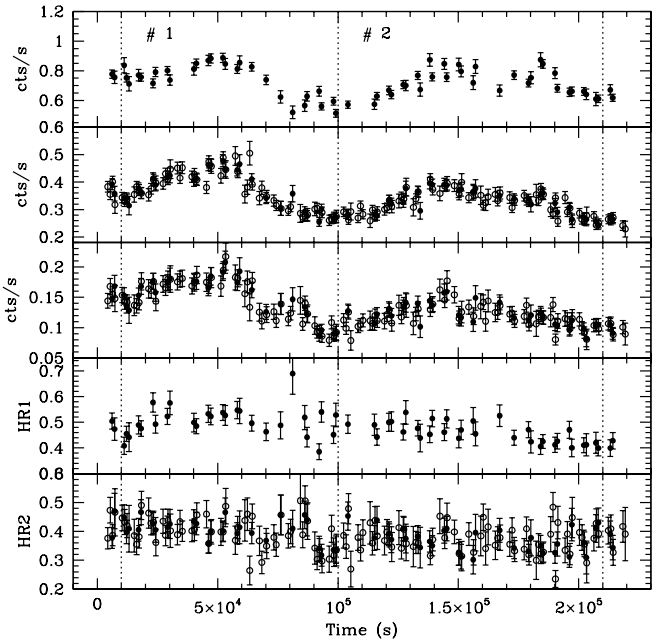


FIG. 3.—Light curves and hardness ratios of the 1999 November 4–6 observation. Data are rebinned over 1000 s. The reference time is 1999 November 4 (TJD = 11,486) 04:00:00. The panels and symbols have the same meanings as those in Fig. 1. This data set is basically divided into two single flares numbered as flare 1 and flare 2.

lowing discussion we briefly describe the global properties of each light curve.

#### 3.1.1. *1996*

PKS 2155−304 was in an intermediate state during this observation. A flare of low amplitude, flare 1, is visible at the beginning of the observation. Flare 2 constitutes the major flare during this campaign. This flare shows an asymmetric structure with different rising ($\sim 5 \times 10^4$ s) and decaying ($\sim 3 \times 10^4$ s) timescales. These timescales may be similar when extending the decay phase to the same level of count rate as the beginning of the rising phase. Moreover, the rising phase shows steeper slope than the decaying one does. This major flare is followed, superimposed on its decay phase, by a lower amplitude flare, flare 3. Another flare occurs toward the end of the observation; unfortunately, only the rising phase was sampled. There are still some small-amplitude flickers superimposed on the overall trend of the flares.

The hardness ratio HR1 shows a behavior similar to that of the light curves, albeit rather marginal, in the sense that the spectrum becomes harder with increasing intensity, while HR2 does not follow any clear trend.

The energy dependence of this light curve is visible when one carefully examines the major flare, i.e., flare 2. It appears that the 0.1–1.5 keV light curve leads the 1.5–3.5 keV one, which in turn lags the 3.5–10 keV one, indicating that the interband time lags may change the sign across the 0.1–10 keV band. This interesting finding will be examined with the cross-correlation (§ 3.6.4) and spectral analysis (§ 4.2.2).

#### 3.1.2. *1997*

The source was in its brightest state during this observation. At the beginning of the observation it exhibits the maximum amplitude of variability (flare 1) among the observations with *BeppoSAX*. The rising phase of flare 1 was not completely sampled. At the end of the flare a fluctuation is significant that is most evident in the highest energy band. In the middle of the observation, a relatively small amplitude flare (flare 2) presents quite similar rising and declining timescales. The duration of this flare is the shortest among the observations studied in this paper. The aspect of flare 3 is different from that of the first two; it is probably the result of convolution of more than one "flare" event.

An overall trend similar to that of the count rates is apparent in hardness ratio HR1, while HR2 does not show any trend.

#### 3.1.3. *1999*

The source was in its faintest state during this observation. The light curve is dominated by two "isolated" flares, which show similar durations of about 1 day. The shapes of the flares are quite different. Flare 1, brighter and more pronounced than flare 2, shows a faster decaying phase than the rising one. In contrast, flare 2 shows a somewhat faster rising phase than the declining phase. The energy-dependent trend is quite evident in both flares. For example, during flare 1, the decaying phase shows a convex shape in the 0.1–1.5 keV band, while a concave shape is clear in the 1.5–3.5 keV band. Flare 2 is peculiar; it appears that the 0.1–1.5 keV light curve consists of two "flares" that are invisible in the two higher energy bands.

It is difficult to discuss the correlation between the evolution of the hardness ratio and that of the light curves because of poor photon statistics in the high-energy bands, resulting in hardness ratios with large error bars.

### 3.2. *Amplitude and Timescales of Variability*

The normalized excess variance $\sigma_{\rm rms}^2$ (see Appendix A for the definition) is intuitively utilized to quantify the amplitude of variability of a light curve. To compare the amplitude of variability in different energy bands, the 0.1–10 keV energy band is divided into four energy bands, i.e., 0.1–0.5, 0.5–2.0 (LECS), 2–4, and 4–10 keV (MECS). The light curves are rebinned over 600 s. This integration time is chosen so that it provides adequate statistical accuracy during the low-intensity state (e.g., 1999), especially for high-energy bands where photon counts are rather low. The bins that are less than 25% exposed are rejected; this assures that each bin has sufficient (more than 20) photons for the Gaussian statistics to be appropriate. The same analysis is repeated with a rebinning over 5670 s (about one satellite orbital period), and the bins that are less than 10% exposed are rejected to ensure adequate signal-to-noise ratio. This binning produces a comparable number of bins in the LECS and the MECS.

The same light curves (over bins and energies) used in estimating the excess variance are further utilized to quantify the "minimum doubling timescale" $T_2$ (see Zhang et al. 1999 for detailed definition). We just remind here that the doubling timescales that have uncertainties (formally propagated) larger than 20% of the value itself are rejected to minimize the risk of contamination by isolated data pairs with large errors and insufficient fractional exposure time.

The results are tabulated in Table 2. Before discussing energy and intensity dependence of $\sigma_{\rm rms}^2$, it is important to know how different samplings affect $\sigma_{\rm rms}^2$. This issue is discussed in detail in Appendix A. The largest uncertainty is the observing duration $T$ since larger $\sigma_{\rm rms}^2$ values are expected for longer integration times. Therefore, it is necessary to normalize different $\sigma_{\rm rms}^2$ values to the same $T$. As discussed in Appendix A, we normalize $T$ values of 1996 and 1997 to that of 1999. The amplification factor for $\sigma_{\rm rms}^2$ is estimated to be $\sim$1.2 and $\sim$2.5 for the 1996 and 1997 observations, respectively. We also discuss in Appendix A the uncertainties due to binning size, the signal-to-noise ratio, and irregular gaps. The determination of the correction factor due to these uncertainties needs detailed simulations. In any case, it is not important for the 5670 s binned light curves since they are evenly sampled and have high signal-to-noise ratios.

From Table 2, one can see that the 1997 values of $\sigma_{\rm rms}^2$ are significantly larger and the values of $T_2$ shorter than those of 1996 and 1999 in all the considered energy bands. Our results show a general trend that $\sigma_{\rm rms}^2$ increases and $T_2$ decreases with increasing energy. There are, however, some exceptions. It seems that the 1996 $\sigma_{\rm rms}^2$ calculated from the 600 s binned light curve keeps constant with energy. The average count rates of 1996 are higher than those of 1999 but show smaller $\sigma_{\rm rms}^2$ in the three high-energy bands. However, in the 0.1–0.5 keV band, the count rates and $\sigma_{\rm rms}^2$ of 1996 and 1999 are statistically indistinguishable.

In summary, PKS 2155−304 shows complex variability, and correlation of $\sigma_{\rm rms}^2$ and $T_2$ with brightness is no longer clear, a result that is different from that obtained by Zhang

TABLE 2
EXCESS VARIANCE AND MINIMUM DOUBLING TIMESCALES OF VARIABILITY

| BAND (keV) | COUNTS PER SECOND | $\sigma^2_{\rm rms}$ ($\times 10^{-2}$) | | | $T_2$ (ks) | |
|---|---|---|---|---|---|---|
| | | 600 s Bin | 5670 s Bin | Corrected 5670 s Bin[a] | 600 s Bin | 5670 s Bin |
| | | | 1996 | | | |
| 0.1–0.5 ..... | 0.34 | $1.52 \pm 0.31$ | $4.08 \pm 0.52$ | 4.90 | $65.4 \pm 12.0$ | $93.7 \pm 18.6$ |
| 0.5–2 ..... | 0.91 | $1.35 \pm 0.20$ | $1.71 \pm 0.37$ | 2.05 | $86.0 \pm 14.5$ | $104.1 \pm 15.6$ |
| 2–4 ..... | 0.72 | $1.48 \pm 0.14$ | $1.79 \pm 0.35$ | 2.15 | $53.5 \pm 12.4$ | $77.8 \pm 11.1$ |
| 4–10 ..... | 0.32 | $1.73 \pm 0.20$ | $3.58 \pm 0.60$ | 4.30 | $35.2 \pm 7.0$ | $59.7 \pm 10.4$ |
| | | | 1997 | | | |
| 0.1–0.5 ..... | 0.55 | $3.28 \pm 0.54$ | $5.71 \pm 1.24$ | 14.28 | $27.8 \pm 4.9$ | $31.0 \pm 4.4$ |
| 0.5–2 ..... | 1.40 | $6.55 \pm 1.19$ | $6.28 \pm 1.54$ | 15.70 | $15.2 \pm 1.7$ | $15.9 \pm 1.5$ |
| 2–4 ..... | 0.80 | $7.29 \pm 1.19$ | $6.89 \pm 1.80$ | 17.23 | $9.16 \pm 1.1$ | $17.5 \pm 2.1$ |
| 4–10 ..... | 0.32 | $8.34 \pm 1.39$ | $11.1 \pm 2.18$ | 27.75 | $5.87 \pm 1.0$ | $14.8 \pm 2.4$ |
| | | | 1999 | | | |
| 0.1–0.5 ..... | 0.33 | $1.60 \pm 0.40$ | $3.81 \pm 0.62$ | ... | $36.9 \pm 6.5$ | $107.4 \pm 15.9$ |
| 0.5–2 ..... | 0.54 | $2.19 \pm 0.31$ | $2.91 \pm 0.69$ | ... | $33.3 \pm 6.1$ | $35.2 \pm 5.3$ |
| 2–4 ..... | 0.27 | $2.75 \pm 0.28$ | $5.25 \pm 0.80$ | ... | $36.3 \pm 6.7$ | $51.2 \pm 9.2$ |
| 4–10 ..... | 0.11 | $4.01 \pm 0.42$ | $15.2 \pm 1.47$ | ... | $19.4 \pm 3.8$ | $31.9 \pm 5.2$ |

[a] Corrected $\sigma^2_{\rm rms}$ of 1996 and 1997 for the 5670 s bin.

et al. (1999). However, the results presented here may be biased by poor photon statistics in some cases.

### 3.3. *Variability of Hardness Ratio*

Before spectral analysis (§ 4), spectral variability versus flux can be simply studied using the hardness ratios as a function of count rates. In Figure 4, we plot the hardness ratio of 2–10 keV/0.1–2 keV versus the observed count rate in the 2–10 keV band for each flare as numbered in Figures 1–3. Each point is binned over 5670 s, and points with less than 10% fractional exposure are rejected to ensure sufficient photons in a bin, as discussed in the previous section. Six flares are shown in the figure. The points with error bars indicate the starting point of each loop, and the solid line tracks the time sequences of development of each flare. In general, they show clockwise hysteresis, as seen from Figure 4, indicating that the low-energy photons lag the high-energy ones, the so-called soft lag. It is worth noting that the flares are generally complicated with the occurrence of smaller amplitude flickers overlapping on the major flares, leading to a break of the clean and smooth loop of hardness ratio versus count rate. For the 1997 flare 1, the loop only starts from the maximum point of the flare because of insufficient sampling of the rising phase of this flare.

Spectral variability will be studied in a more accurate way with the time-resolved spectral analysis in § 4. The feature of the soft lag deduced from the clockwise pattern of the loops of hardness ratio versus count rate will be quantified with the cross-correlation techniques in § 3.6.

### 3.4. *Power Spectral Density Analysis*

Power spectral density (PSD) is the most common technique to characterize the variability of a source. However, the light curves obtained with *BeppoSAX* are insufficient to perform a fully sampled PSD analysis with the standard means because of the presence of the periodic data gaps (see § 2). We calculate the normalized power spectral density (NPSD) following the method of Hayashida et al. (1998), which utilizes the standard discrete Fourier transform (see Appendix B for the definition). To ensure that this method is appropriate, evenly sampled data sets are required. We therefore made 2–10 keV (MECS) light curves with two kinds of bin sizes, 256 and 5670 s. The light curve binned over 5670 s is evenly sampled for each observation, except for the last part of 1996, which is rejected because of a long gap not due to the Earth occultation. The light curve binned over 256 s is divided into a series of individual segments based on the orbital period. The segments that have no gaps are used to ensure that each segment is evenly sampled.

The light curve binned over 5670 s produces the NPSD in the low-frequency (less than $2 \times 10^{-4}$ Hz) range. Similarly, each segment of the light curve binned over 256 s yields one set of $[f, p(f)]$ values in the high-frequency (larger than $2 \times 10^{-4}$ Hz) range, which are first sorted in frequency and then averaged for the same frequency. The NPSDs of both the low- and the high-frequency range are then rebinned in a logarithmic interval of 0.2 (i.e., a factor of 1.6) to allow the determination of errors. The disadvantage of this technique is that it introduces a large gap in the NPSD around $2 \times 10^{-4}$ Hz.

The NPSDs obtained with this procedure are shown in Figure 5. One can see that each NPSD generally follows a very steep power-law shape that quickly decreases with increasing frequency in the low-frequency range. It is important to note that pronounced differences exist among the three NPSDs. The power-law slope of the 1997 NPSD may extend to $10^{-3}$ Hz, indicating rapid variability on a timescale of $\sim$1000 s. However, power-law breaks of the 1996 and 1999 NPSDs are clear before $10^{-3}$ Hz, while this feature may be overwhelmed by the poor photon statistics when the source is in the fainter states.

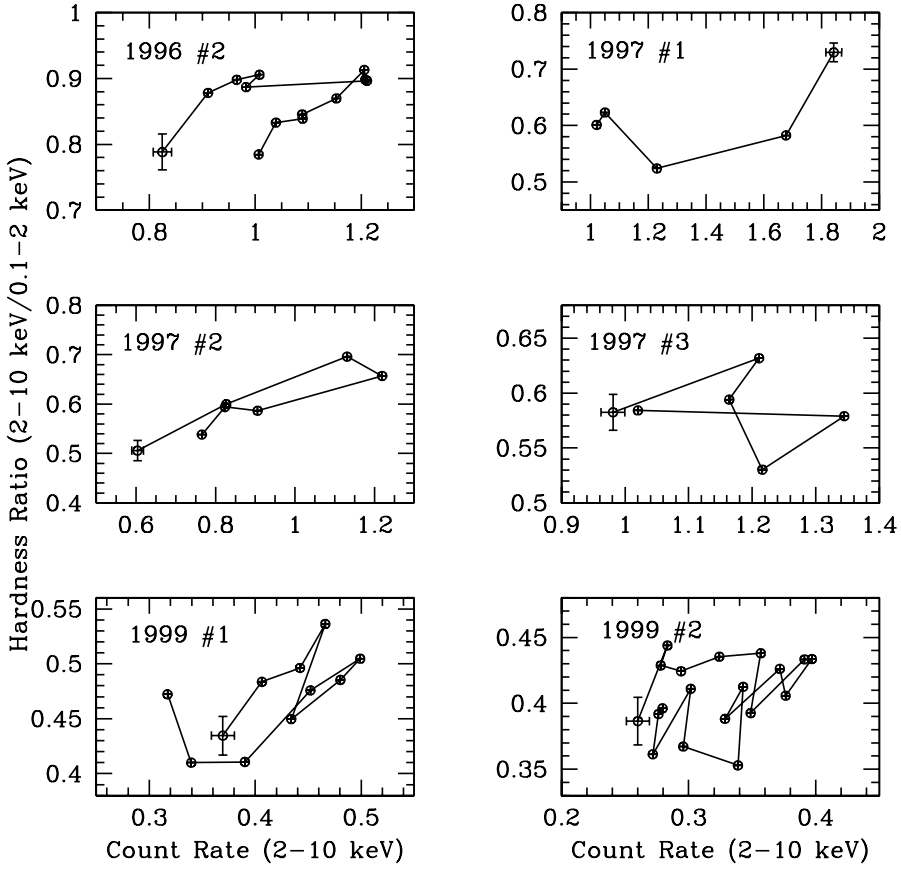


FIG. 4.—Hardness ratio of the 2–10 keV to 0.1–2 keV bands as a function of the observed count rate in the 2–10 keV band. The data are binned over 5670 s. The point with error bars represents the starting point of the loop. The errors shown are typical.

To quantify the slope, we fit each NPSD with a single power-law model; the best-fit parameters are reported in Table 3. The strong red noise variability nature is indicated by the steep slopes of ∼2–3. The best-fit power-law slope shows that the NPSD of 1997 is flatter than those of 1996 and 1999, but the differences are statistically weak because of quite large errors associated with the slopes of the 1996 and 1999 NPSDs.

Finally, we compare the NPSDs presented here with those derived by Zhang et al. (1999), where the gap-filling technique was used to estimate the PSDs of the 1996 and 1997 observations. We found that the 1997 NPSD calculated with the gap-filling method is fully consistent with that given here. For the 1996 observation, however, it seems that the PSD slope derived with the gap-filling method is flatter than that obtained here, but when the large errors of the NPSD are taken into account, we believe that the 1996 slopes calculated with the two methods are also consistent. Moreover, we note that " red noise leak " could be reduced after linearly interpolating across the gaps, but Poisson errors associated with these fitted points are still uncertain. The true shape of PSDs may be distorted by the sampling window function. It is also necessary to point out that the PSDs derived in Zhang et al. (1999) were averaged by dividing the whole light curves into several intervals.

TABLE 3
THE BEST-FIT PARAMETERS OF NPSD

| Observation | $N$ (at $10^{-4}$ Hz)[a] ($Hz^{-1}$) | $\alpha$[a] | $\chi^2$(dof) |
|---|---|---|---|
| 1996 ..... | $0.38 \pm 2.13$ | $2.94 \pm 0.52$ | 5.14(8) |
| 1997 ..... | $20.83 \pm 24.72$ | $1.93 \pm 0.15$ | 5.99(8) |
| 1999 ..... | $0.35 \pm 3.01$ | $3.10 \pm 0.76$ | 8.64(9) |

NOTE.—The power-law model is assumed to be $P(f) = N(f/10^{-4})^{-\alpha}$.
[a] The errors are 1 $\sigma$.

### 3.5. *Structure Function Analysis*

With respect to PSD, the structure function (SF; see Appendix C for the definition) technique has advantages in quantifying the time variability of an unevenly sampled light curve. One of the most powerful features of SF analysis is the ability to discern the range of the timescales that contribute to the variations of a source. The most important one is $\tau_{max}$, at which the SF flattening occurs.

The light curves are binned over 1000 s and normalized by the mean count rate before calculating the SF. In this way, the SF is normalized by the squared mean count rate of the light curve, allowing us to compare SFs in different states of a source. The SFs are calculated for the 0.1–2 keV (LECS) and 2–10 keV (MECS) energy bands to compare the variability characteristics in the soft and hard X-ray bands. The contribution of the measurement (Poisson) noise to the SFs is $2\sigma^2_{noise}$, which is subtracted. Figure 6 shows the derived SFs. It is necessary to point out that the 0.1–2 keV SFs are more poorly constrained than the 2–10

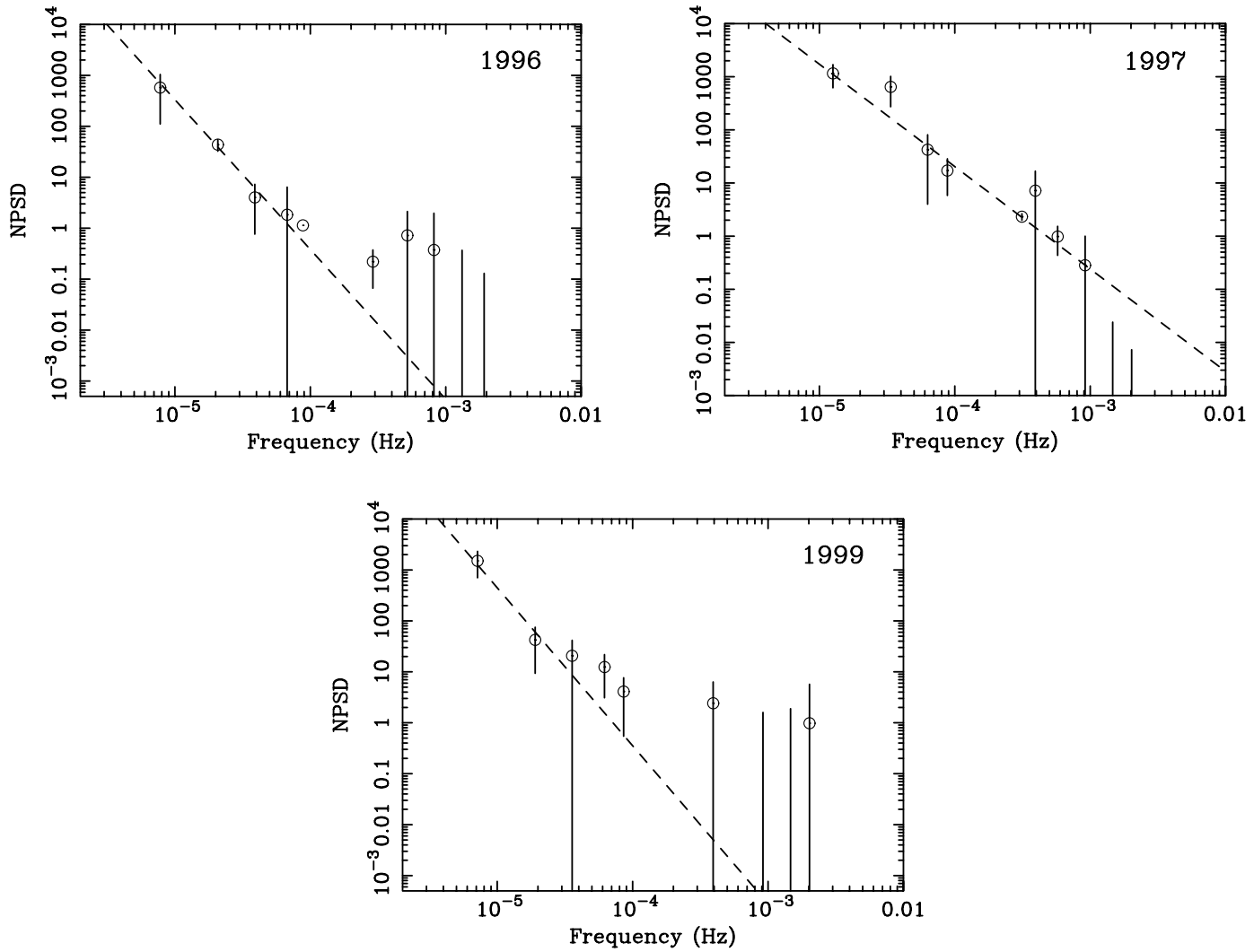


FIG. 5.—NPSD derived from the light curves in the 2–10 keV band. The dashed line corresponds to the best fit with a power-law model.

keV ones because of the low exposure efficiency of the LECS.

The first piece of information we got from the SFs of the three campaigns is that they show similar structures. The variations of PKS 2155−304 decrease quickly with decreasing timescales, as seen from the steep slopes of the SFs. Similar to NPSDs, 1996 and 1999 SFs may show evidence for the shortest correlation timescales $\tau_{\rm min}$ of around 6000 s, while $\tau_{\rm min}$ could be $\sim$1000 s or even lower in 1997. This feature also indicates that PKS 2155−304 tends to be more rapidly variable in the high state, but as for PSD, this difference may be overwhelmed by strong Poisson noise in its faint states.

With respect to the PSD, the most important inference from the SFs is that one can determine the longest correlation timescale $\tau_{\rm max}$ identified by the first "turnover" point at the end of the long timescale of the power-law shape. Importantly, $\tau_{\rm max}$ may reflect the typical (half-)duration time of the repeated flares; $\tau_{\rm max}$ thus may give an evaluation of the characteristic timescale of the source. To accurately quantify $\tau_{\rm max}$ and the power-law slope, a broken power-law model

$$\mathrm{SF}(\tau) = C\left(\frac{\tau}{\tau_{\rm max}}\right)^{\beta}, \quad \tau \le \tau_{\rm max}\ ,$$

$$\mathrm{SF}(\tau) = C\left(\frac{\tau}{\tau_{\rm max}}\right)^{\beta_1}, \quad \tau > \tau_{\rm max}$$

is fitted to the SF between 1000 s and the timescale at which the first minimum occurs. The best-fit curves are plotted in Figure 6 with solid lines, and the best-fit parameters with a 90% confidence region for one interesting parameter are tabulated in Table 4, where only the first power-law slope $\beta$ and $\tau_{\rm max}$ are shown. The results show that the power-law slopes of the SFs are $\sim$1–1.5; this corresponds to a PSD power-law slope of $\sim$2–2.5, suggesting that the X-ray variability of PKS 2155−304 is always dominated by shot noise. Moreover, our results suggest that $\tau_{\rm max}$ differs by a factor of $\sim$6 from epoch to epoch. This may shed light on some clues on the dynamics and the structure of the jet (see § 5.2).

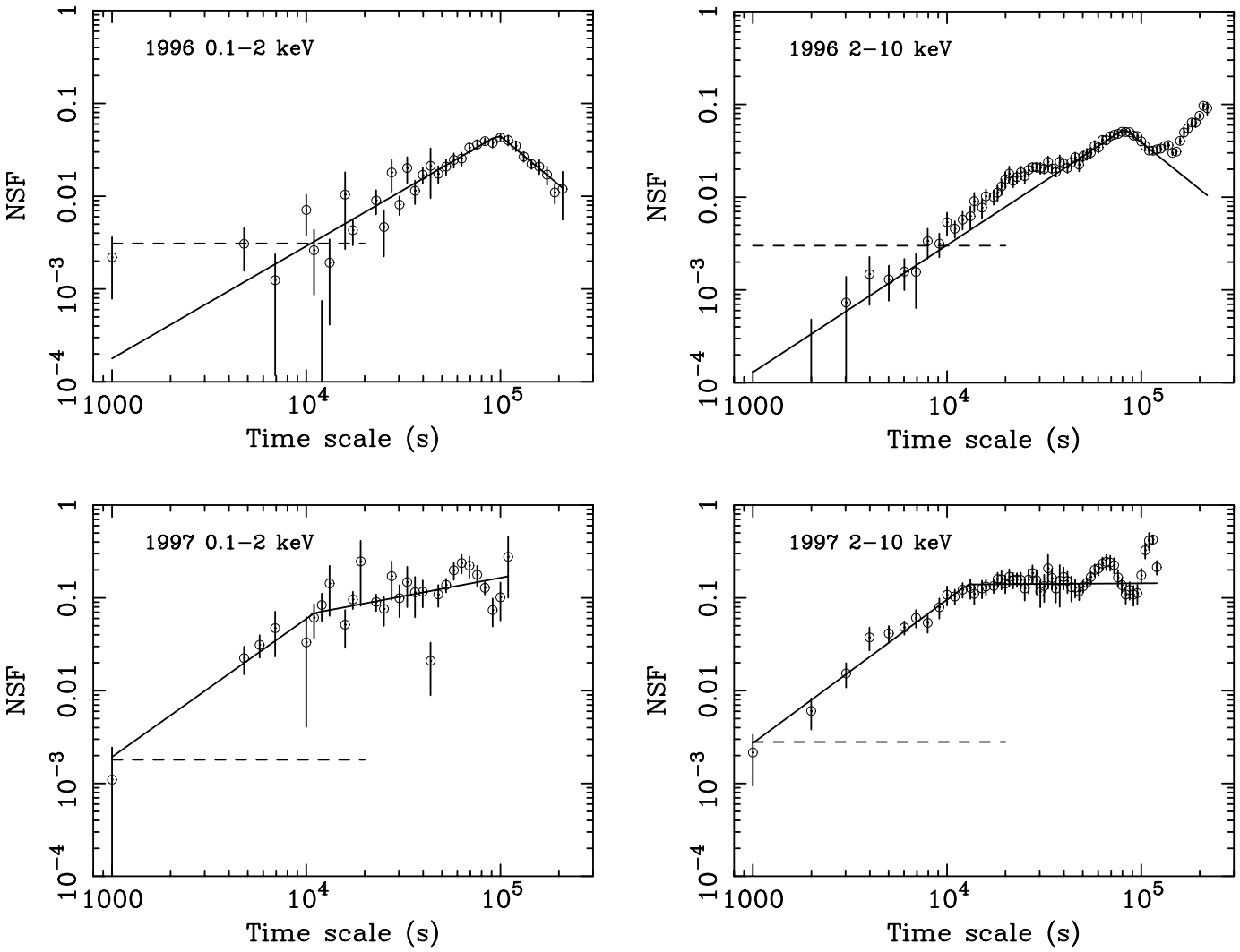


FIG. 6.—Normalized SF derived from the 1996 (*top*), 1997 (*middle*), and 1999 (*bottom*) 1000 s binned light curves in the 0.1–2 keV (*left*) and 2–10 keV (*right*) bands. Solid lines are the best fits with a broken power-law model, and the dashed lines are the level of measurement noise, $2\sigma^2_{\rm noise}$, which is subtracted from the SFs.

### 3.6. *Cross-Correlation Analysis*

The main goal of the cross-correlation analysis is to determine the degree of correlation and the time lags between the variations in different energy bands. Before constructing the cross-correlation function (CCF), light curves are normalized to zero mean and unit variance by subtracting the mean count rate and dividing by the rms of the light curves (see, e.g., Edelson et al. 2001). CCFs are measured using two techniques suited to unevenly sampled time series: the discrete correlation function (DCF; Edelson & Krolik 1988) and the modified mean deviation (MMD; Hufnagel & Bregman 1992). In addition, model-independent Monte Carlo simulations taking into account "flux randomization" (FR) and "random subset selection" (RSS) of the data sets (Peterson et al. 1998) are used to statistically determine the significance of time lags derived from the DCF and MMD. FR/RSS is based on a computationally intensive statistical "bootstrap" method. This will build a cross-correlation peak distribution (CCPD; Maoz & Netzer 1989). For details of this procedure, we refer to Zhang et al. (1999). In most cases, the bin sizes of light curves and the DCF/MMD are chosen to be about 3 times smaller than the possible lag after a series of experiments. The DCF/MMD is fitted with a Gaussian function plus a constant, and the time lags are evaluated with the Gaussian centroid rather than the DCF/MMD peak/dip to reduce the possibility of spurious estimates of time lags due to a particular DCF/MMD point that could originate from statistical errors and data gaps

TABLE 4
THE BEST-FIT PARAMETERS OF STRUCTURE FUNCTIONS

| | $\beta$[a] | | $\tau_{\rm max}$ ($\times 10^4$ s)[a] | |
|---|---|---|---|---|
| OBSERVATION | 0.1–2 keV | 2–10 keV | 0.1–2 keV | 2–10 keV |
| 1996 | $1.21^{+0.38}_{-0.38}$ | $1.37^{+0.21}_{-0.24}$ | $9.81^{+0.27}_{-0.63}$ | $8.20^{+0.35}_{-0.34}$ |
| 1997 | $1.49 \pm 0.30$[b] | $1.55^{+0.21}_{-0.21}$ | $1.10 \pm 0.35$[b] | $1.28^{+0.38}_{-0.19}$ |
| 1999 | $0.99^{+0.12}_{-0.11}$ | $1.33^{+0.08}_{-0.08}$ | $6.55^{+0.27}_{-0.72}$ | $6.17^{+0.33}_{-0.35}$ |

[a] The errors are 90% confidence level for one parameter of interest.
[b] 1 $\sigma$ errors due to the SF too insensitive to derive the 90% confidence level.

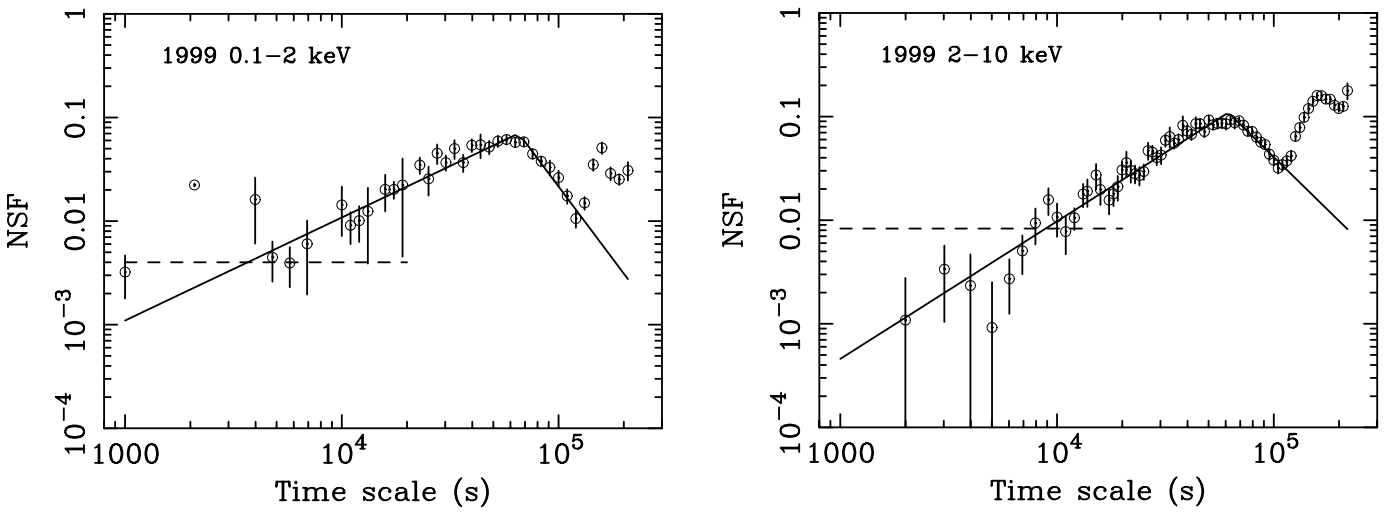


FIG. 6.—*Continued*

(see Zhang 2000 for details). The accuracy of a cross-correlation result can be better than the typical binning as long as the DCF/MMD functions involved are reasonably smooth. Throughout the paper, a positive lag indicates that the lower energy photons lag the higher energy ones (soft lag), while a negative lag represents the opposite (hard lag).

We first comment on some issues that may affect the evaluations of time lags. The detection of a time lag is dependent not only on the sampling characteristics of the light curves but also on the specific variations and the measurement uncertainties of the light curves. The increasing level of the measurement uncertainties with respect to real variability will broaden the CCPD built from Monte Carlo simulations, and this will decrease the confidence of the detection of a time lag. The detection of a time lag is thus mainly sensitive to a pronounced flare in which the relative level of the measurement uncertainties tends to be minimum. In addition, a light curve generally shows multiple flares that can be dominated by different timescales, as discussed in § 5.2; different interband time lags are then expected from flare to flare. Cross-correlating the entire light curve may prevent the clear detection of a time lag since it only gives a mean value of more than one time lag corresponding to the respective flares. In the worst case the average of the positive and negative time lags may lead to nondetection of a time lag. To obtain a proper determination of a time lag, from the point of view of physical processes, one must analyze each flare individually rather than the whole light curve. However, the statistical confidence of a cross-correlation result decreases because the duration of a single flare is generally much shorter than that of the whole light curve. Since the results for the 1996 and 1997 data sets presented in Zhang et al. (1999) were based on the whole light curves, we reanalyze them along with the 1999 data set following this criterion. As we will show in the following subsections, the values of time lags depend significantly on the different parts of the light curve that are cross-correlated.

The time lags derived with the DCF/MMD for the six flares indicated in Figures 1–3 are reported in Table 5. Only the time lags between the 0.1–1.5 keV and 3.5–10 keV energy bands are shown. It is worth noting that the differences in the results obtained using the DCF and MMD techniques are significant in some cases (e.g., for the 1999 flare 2); these differences are mainly caused by the irregularities of the DCF/MMD that results in large uncertainties when fitting the DCF/MMD with a simple Gaussian function. It can be seen that the source shows soft lags in all flares, while the values of soft lags are different from flare to flare, ranging from a few hundred seconds to about 1 hr. If one compares the values of soft lags with the duration of the flares or, more precisely, with $\tau_{\max}$ inferred with the SFs (see Table 4), one can find that there may be a correlation between them; i.e., smaller soft lags seem to be associated with the flares of shorter duration.

#### 3.6.1. *1996*

We found a soft lag of ~4 hr (between the 0.1–1.5 keV and 3.5–10 keV energy band) evaluated with the whole 1996 observation (Zhang et al. 1999). We recalculate DCF/MMD for the three parts of the light curve as indicated in Figure 1. The time lags of the flare 1 and flare 3 parts cannot be well determined because there is no proper DCF/MMD defined, possibly due to sparse sampling. The flare 2 part, the major flare during this campaign, shows a clear soft lag: $6.16^{+1.38}_{-1.33}$ ks (DCF) and $5.09^{+4.98}_{-3.95}$ ks (MMD). The confidence range of this value at the 1 $\sigma$ level based on FR/RSS simulations is [1.7, 9.3] ks (DCF) and [0.6, 11.8] ks (MMD). It is important to note that the soft lag derived from this major flare is just about half of the soft lag derived from the whole

TABLE 5

TIME LAGS (KS) BETWEEN THE 0.1–1.5 AND 3.5–10 keV BANDS

| Flare | DCF[a] | MMD[a] |
|---|---|---|
| 1996 2..... | $6.16^{+1.38}_{-1.33}$ | $5.09^{+4.98}_{-3.95}$ |
| 1997 1..... | $0.41^{+0.40}_{-0.40}$ | $2.07^{+2.64}_{-1.02}$ |
| 1997 2..... | $0.45^{+0.39}_{-0.29}$ | $0.38^{+0.26}_{-0.46}$ |
| 1997 3..... | $1.68^{+0.52}_{-0.39}$ | ... |
| 1999 1..... | $3.50^{+1.06}_{-1.05}$ | $3.03^{+1.74}_{-1.77}$ |
| 1999 2..... | $4.72^{+2.62}_{-2.61}$ | $6.93^{+4.25}_{-4.13}$ |

[a] The errors are 90% confidence level for one parameter of interest.

observation, demonstrating strong dependence of the estimate of the time lag on the examined part, basically containing a single flare, of the observed light curve.

#### 3.6.2. *1997*

The whole 1997 observation is characterized by a soft lag of ∼1 ks between the 0.1–1.5 and 3.5–10 keV bands (Zhang et al. 1999). This light curve can be divided into three flares with durations of ∼40 ks each (Fig. 2). Thanks to their brightness, we can make a proper estimate of the time lags for each flare. The first two flares show quite small soft lags of a few hundred seconds, with the lower limit down to zero lags. The soft lag of the third flare is significant when determined with the DCF (∼1600 s) but not with the MMD (no proper MMD function exists). FR/RSS simulations are not performed because of the short duration of the flares, but we refer to Zhang et al. (1999) for the simulations based on the whole light curves.

#### 3.6.3. *1999*

With respect to the previous two campaigns, PKS 2155−304 is in its faintest state during this observation. Of interest is that two "isolated" flares were completely sampled, allowing us to study in detail the interband correlations and the time lags occurring in the faint state of the source.

The DCF/MMD between the 0.1–1.5 keV and 3.5–10 keV bands are shown in Figure 7. Flare 1 has a relatively well-defined DCF/MMD, and the correlation between the two energy bands is high, ∼0.8, as seen from the centroid of Gaussian fit to the DCF. Both DCF and MMD suggest a soft lag of about 3 ks. FR/RSS simulations indicate that the confidence (1 $\sigma$) range of this soft lag is [2.7, 11.6] ks (DCF) and [1.3, 12.2] ks (MMD).

The DCF/MMD of flare 2 does not present a well-defined function. The DCF suggests a very low correlation of about 0.2, indicating that the variations of the soft and hard photons are weakly correlated. This might be expected already from the light curves (Fig. 3): in the 0.1–1.5 keV band there might be two flares, which are not seen in the 3.5–10 keV band. Therefore, the cross-correlation analysis can only give an indication of the interband time lags, which does not necessarily give a clean and unambiguous measure of the relationship between the two time series. FR/RSS simulations result in broader CCPDs of this soft lag, which

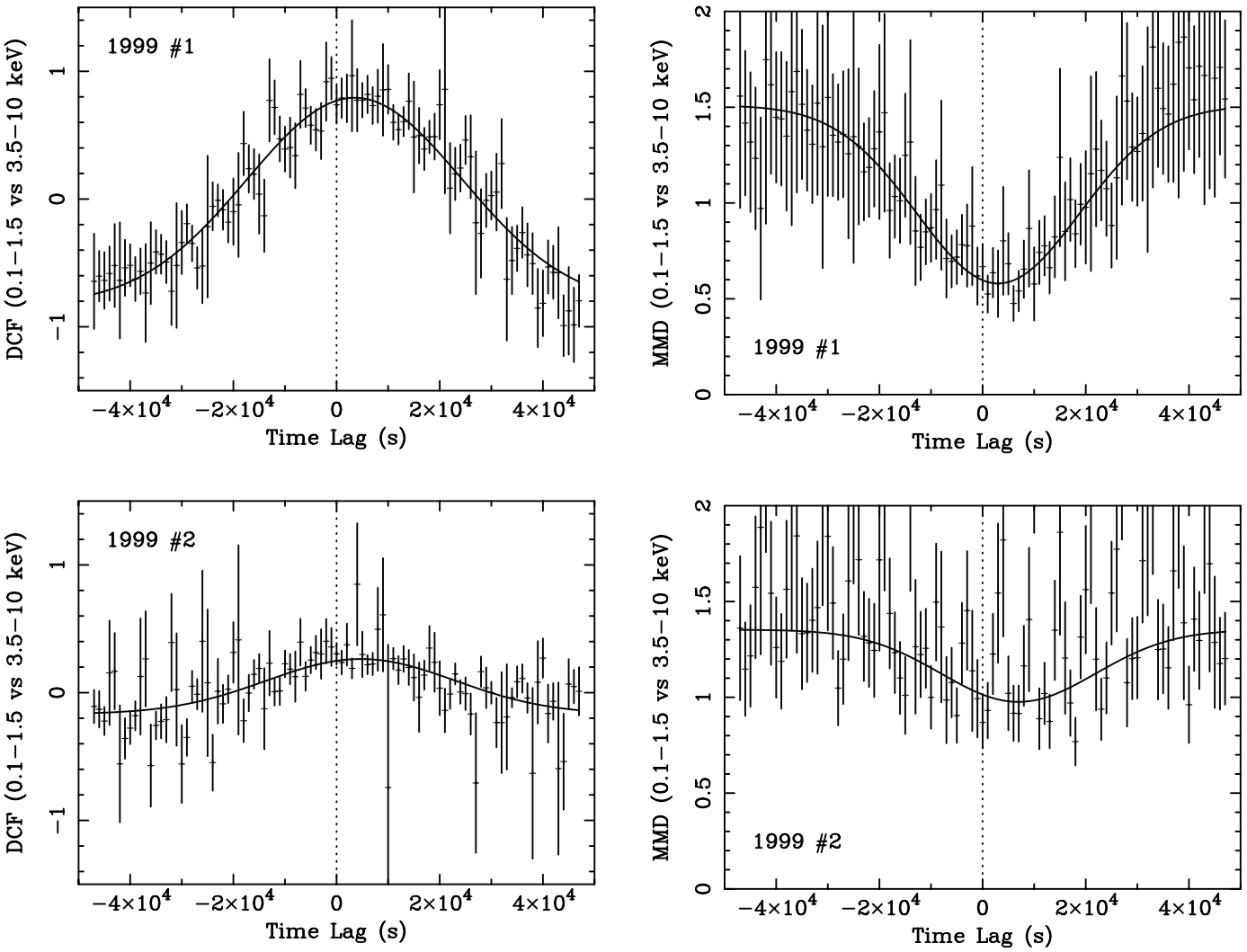


FIG. 7.—DCF (*left*) and MMD (*right*) between the 0.1–1.5 keV and the 3.5–10 keV bands derived from the 1999 flare 1 (*top*) and flare 2 (*bottom*). The solid curve indicates the best fit consisting of a Gaussian function plus a constant.

are [0.3, 11.0] ks (DCF) and [3.7, 13.7] ks (MMD) at the 1 $\sigma$ confidence level.

Finally, as we commented on above, the CCPDs are strongly broadened because of weak statistics of photons. This gives estimates of the soft lags with low confidence.

#### 3.6.4. *Energy Dependence of Soft Lags*

We further quantify the energy dependence of soft lags by dividing the 0.1–10 keV energy band into six narrow energy bands, i.e., 0.1–0.5, 0.5–1.0, 1.0–1.5 (LECS), 1.5–2 (LECS and MECS), 2–4, and 4–10 keV (MECS), and we measure the soft lags for each flare with respect to the 4–10 keV energy band. This is an important issue to test the synchrotron cooling mechanism.

The results are shown in Figure 8 for the 1996 flare 2, 1999 flare 1, and 1999 flare 2. The energy dependence of soft lags for the three flares of 1997 cannot be determined because of the short duration and the small soft lags. Further observations with higher time resolution may determine the energy dependence of very small time lags that are probably associated with the flares of short duration.

The soft lags of the variations of the soft X-rays with respect to those of the hard X-rays are thought to be due to the energy dependence of synchrotron cooling time $t_{\rm cool}$ of relativistic electrons responsible for the emission in the studied energy bands, which results in the dependence of $t_{\rm cool}$ on the emitting photon energies (see § 5.2). Therefore, the observed energy dependence of the soft lags can be fitted with equation (8), which will give a constraint to the magnetic field $B$ and the Doppler factor $\delta$ of the emitting regions in the form of $B\delta^{1/3}$ (see also eq. [10]). The best fits are shown in Figure 8 with dashed lines and give $B\delta^{1/3} = 0.40$, 0.37, and 0.40 G for the 1996 flare 2, 1999 flare 1, and 1999 flare 2, respectively.

For the 1996 flare 2, our analysis reveals that, with respect to the 4–10 keV band, the soft lag of the 0.1–0.5 keV band is significantly smaller than those of other low-energy bands (see Fig. 8*a*); this suggests that the 0.1–0.5 keV photons may lead the other low-energy photons. This point has already been noted in the light curves (see § 3.1.1). Therefore, in this flare PKS 2155−304 may show evidence of a hard lag in the soft X-rays and a soft lag in the hard X-rays. This is the first time that a blazar shows opposite behavior of the interband

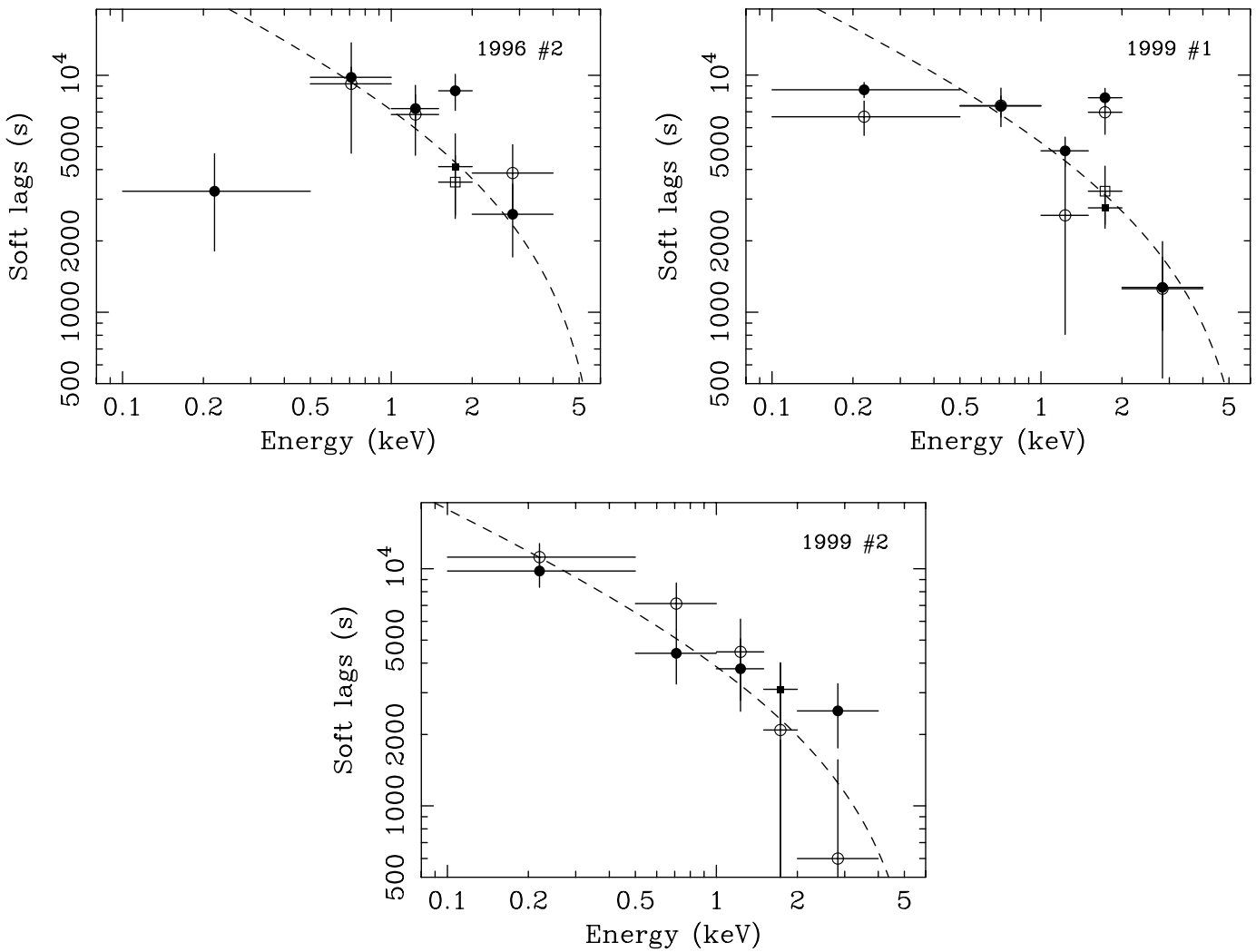


FIG. 8.—Soft lags, measured with respect to the 4–10 keV band, as a function of photon energies. The dashed curve is the best fit with the energy dependence of the synchrotron cooling timescale. The results with DCF and MMD are indicated with the solid and open symbols, respectively. Note that the soft lags in the 1.5–2 keV band are derived from both the LECS (*circles*) and the MECS (*squares*).

time lags in the different energy bands, which demonstrates the complexity of the variability of the source.

## 4. SPECTRAL ANALYSIS

Spectral analysis for the 1996 and 1997 data sets was presented in Giommi et al. (1998) and Chiappetti et al. (1999), respectively, but neither paper examined detailed spectral evolution. To reveal in detail the spectral variability of PKS 2155−304, in particular during individual flares and between the flares, we perform again a time-resolved spectral analysis for the 1996 and 1997 data sets along with the new 1999 data set. To do so, we divide each data set into subsegments on the basis of a single *BeppoSAX* orbit or a multiple of it to reach sufficient statistics for each segment. The main goal of such an analysis is to produce homogeneous spectral information of PKS 2155−304 to study flare-dependent spectral evolution, which is, together with temporal variability, essential to understanding and constraining the jet physics of the source.

Because of remaining calibration uncertainties, in the spectral analysis LECS and MECS data have been considered only in the ranges 0.1–3 keV and 1.6–10 keV, respectively. These "good" spectral channels (i.e., channels 11–285 for the LECS and 36–220 for the MECS) are further rebinned using the grouping templates available at the *BeppoSAX* SDC. Because of the very steep spectral shape of this source, we modified the MECS grouping template above ~7 keV in order to have sufficient photons in each new bin.

Spectral analysis is performed with the XSPEC, Version 11.1, package, using the latest available calibration files (i.e., response matrices and effective areas) and blank-sky fields. The background spectra for each observation have been evaluated from these blank-field event files by applying the same extraction region as the source spectra; i.e., the extraction position and radii are identical for both the source and the background spectra.

The Galactic absorption column in the direction of PKS 2155−304 ($N_{\rm H} = 1.36 \times 10^{20}$ cm$^{-2}$; Lockman & Savage 1995) is used during the spectral fits. Because of a small mismatch in the cross-calibration between the LECS and the MECS, we add a free multiplicative constant factor in the fit procedure to allow a variable normalization between the LECS and the MECS data. The acceptable range of this constant is 0.7–1.0, which depends mainly on the source position on the detectors (see Fiore et al. 1999).

### 4.1. *Spectral Models*

The observed X-ray spectra of blazars are usually thought to be represented by a single power-law model. However, since PKS 2155−304 (and other TeV sources) tends to show continuously downward-curved spectra, a model consisting of a single power law plus free low-energy absorption or one fixed at a Galactic value generally gives a very poor fit to the LECS+MECS spectra of most segments. Therefore, we will not discuss in detail spectral fits with a single power law. We then test a spectral model consisting of a broken power law with a free absorbing column density or fixed at a Galactic value. This model gives a statistically acceptable minimum reduced $\chi^2$ in each of the fits.

We further apply a continuously curved model (see, e.g., Tavecchio, Maraschi, & Ghisellini 1998) as formulized by Fossati et al. (2000b). This model is described as

$$F(E) = KE^{-\alpha_{-\infty}} \left[1 + \left(\frac{E}{E_B}\right)^f\right]^{(\alpha_{-\infty}-\alpha_{+\infty})/f},$$

where $\alpha_{-\infty}$ and $\alpha_{+\infty}$ are the asymptotic values of spectral indices for $E \ll E_B$ and $E \gg E_{\rm B}$, respectively, while $E_B$ and $f$ determine the scale length of the curvature. This model is constrained by four parameters ($\alpha_{-\infty}$, $\alpha_{+\infty}$, $E_B$, $f$).

This function is better understood in terms of the local spectral indices at finite values of $E$ instead of the asymptotic ones. The available parameters of this spectral model are then reexpressed as ($E_1$, $\alpha_1$, $E_2$, $\alpha_2$, $E_B$, $f$) instead of ($\alpha_{-\infty}$, $\alpha_{+\infty}$, $E_B$, $f$), where $\alpha_i$ is the spectral index at energy $E_i$ ($i = 1, 2$). The relationship between these two sets of parameters can be obtained by differentiating the above function to obtain the local spectral indices (for more details, see Fossati et al. 2000b). Since there are two more parameters in the new description of this model, we have to fix one for each of the pairs ($E_1$, $\alpha_1$) and ($E_2$, $\alpha_2$) in order to have a meaningful use of this spectral description. It is interesting to note that it is this degeneracy that determines some advantages of this improved model. In particular, it allows us to derive a local spectral index by setting $E_i$ at a preferred value or the energy of a certain spectral index by setting $\alpha_i$ at the desired value. The most important aspect is the possibility of estimating the position of the peak [as seen in the $\nu$-$\nu F_\nu$, i.e., $E$-$EF(E)$, representation] of the synchrotron component $E_{\rm peak}$ (if it falls within the observed energy band), one of the crucial physical quantities in blazar modeling. This can be obtained by setting one spectral index, i.e., $\alpha = 1$, and leaving the corresponding energy $E$ free to vary in the fit: the best-fit value of $E_{\alpha=1}$ gives $E_{\rm peak}$.

### 4.2. *Results*

Since the curved model presents more useful information than the broken power-law model does, our following discussions focus on the results from the former model, although the latter also gives statistically acceptable fits.

Following Fossati et al. (2000b), to estimate the really interesting parameters, i.e., spectral index at preferred energies and peak energy, we first estimate a proper value of parameter $f$ for each epoch. This is done by allowing all parameters but $N_{\rm H}$ to freely vary in the fit of the time-averaged spectra extracted from each data set. The value of $f$ corresponding the best fit is $2.34 \pm 0.52$, $1.82 \pm 0.37$, and $0.91 \pm 0.86$ for the 1996, 1997, and 1999 data sets, respectively. So $f = 2$ is fixed for the 1996 and 1997 data sets, and $f = 1$ for the 1999 one. With $f$ fixed, the spectrum of each segment has been fitted a few times in order to derive spectral indices at desired energies and $E_{\rm peak}$ (the errors are derived with a 68% confidence level for one parameter of interest). The fluxes have been computed in the 0.1–2 keV and 2–10 keV energy ranges and corrected for Galactic absorption.

#### 4.2.1. *Peak Energies and Spectral Variability*

The source revealed a large flux variability, a factor of ~10 in the 2–10 keV energy band, ranging from $15.1 \times 10^{-11}$ (1997 maximum) to $1.8 \times 10^{-11}$ (1999 minimum) ergs cm$^{-2}$ s$^{-1}$. Such flux changes were accompanied by changes of spectral curvature characterized by the shifts of the peak energy of the synchrotron component as seen in

the $\nu$-$\nu F_\nu$ diagram. Figure 9*a* shows the SED derived from the segment with the maximum flux of each data set. Unfolded spectra have been corrected for low-energy absorption assuming $N_{\rm H}$ equal to the Galactic value. Spectral convexity and shift-of-peak energy are apparent, while $E_{\rm peak}$ values of the 1996 and 1999 spectra may be below the X-ray band. It is worth noting the difference between the 1996 and 1999 spectra: both show similar fluxes in the soft-energy band, while the 1996 spectrum shows higher flux than the 1999 one at energies higher than 0.5 keV.

We show in Figure 9*b* $E_{\rm peak}$ versus the 2–10 keV flux. There is a suggestion that $E_{\rm peak}$ shifts to higher energy with increasing flux, but this trend is clearly dominated by the upper limits of $E_{\rm peak}$. $E_{\rm peak}$ carries direct information on the source's physical properties; however, they are very weakly constrained because of two facts: the signal-to-noise ratio is not good enough and, more importantly, $E_{\rm peak}$ of PKS 2155−304 is around or below the *BeppoSAX* lower energy limit, 0.1 keV. A proper determination of $E_{\rm peak}$ in PKS 2155−304 will depend on the combined UV and soft X-ray spectrum together. In fact, among the 56 data segments, in only three cases can the curved model determine $E_{\rm peak}$ with reasonable accuracy; these correspond to the brightest segments in 1997. In most cases only an upper limit on $E_{\rm peak}$ could be determined.

In Figure 10*a* we show the relationship of the spectral index $\alpha$ at 5 keV and the flux. One can see that there is little correlation between them. In Figure 10*b* we have plotted the spectral index at 0.5 keV against the spectral index at 5 keV. Again, this plot does not show any clear correlation; in particular, each data set is clustered. These results indicate that, on the long epochs, the spectral changes in the soft and hard-energy range do not depend on each other. However, for each data set, this inference could be biased because of large errors on the spectral index. As a comparison, we compute the unweighted average spectral index at 0.5 and 5 keV for the three data sets: $\langle\alpha_{0.5\,\rm keV}\rangle^{1996} = 1.22 \pm 0.07$ and $\langle\alpha_{5\,\rm keV}\rangle^{1996} = 1.77 \pm 0.07$, $\langle\alpha_{0.5\,\rm keV}\rangle^{1997} = 1.09 \pm 0.07$ and $\langle\alpha_{5\,\rm keV}\rangle^{1997} = 1.91 \pm 0.11$, and $\langle\alpha_{0.5\,\rm keV}\rangle^{1999} = 1.47 \pm 0.05$ and $\langle\alpha_{5\,\rm keV}\rangle^{1999} = 2.00 \pm 0.12$. The average spectral curvature from 0.5 to 5 keV is $\Delta\alpha^{1996} = 0.55$, $\Delta\alpha^{1997} = 0.82$, and $\Delta\alpha^{1999} = 0.53$. The large spectral steepenings inferred in the X-ray band should be ascribed to the large steepenings of the (radiating) electron energy distribution because of fast cooling of high-energy electrons.

#### 4.2.2. *The Sign of Time Lags*

For each flare, spectral variability versus flux is further studied with the diagram of $\alpha$-$F$ whose property is that a soft and hard time lag, during a flare, can be qualitatively determined with a clockwise and counterclockwise loop, respectively. In Figure 11 we have plotted the spectral index at 0.5 and 5 keV versus the 0.1–2 keV and 2–10 keV absorption-corrected flux, respectively. The first point of each loop, representing the segment number of each data set, has been numbered. As a further aid to clarity, points are sequentially linked with a solid line in its original time order. The overall behavior of each flare is briefly summarized as follows:

*1996 flare 2*.—A normal clockwise loop, corresponding to the soft lag, is indicated by the $\alpha_{5\,\rm keV}$-$F$ loop, but it shows small changes of spectral index, $\Delta\alpha_{5\,\rm keV} \simeq 0.1$, apart from the second point that hardens from $\alpha \simeq 1.8$ to 1.6. However, a counterclockwise loop, corresponding to the hard lag, is indicated by the $\alpha_{0.5\,\rm keV}$-$F$ relation. This is the first time that an $\alpha$-$F$ loop of a TeV source shows opposite behavior in the soft and hard X-ray bands. Note that such behavior is in agreement with the results obtained from the

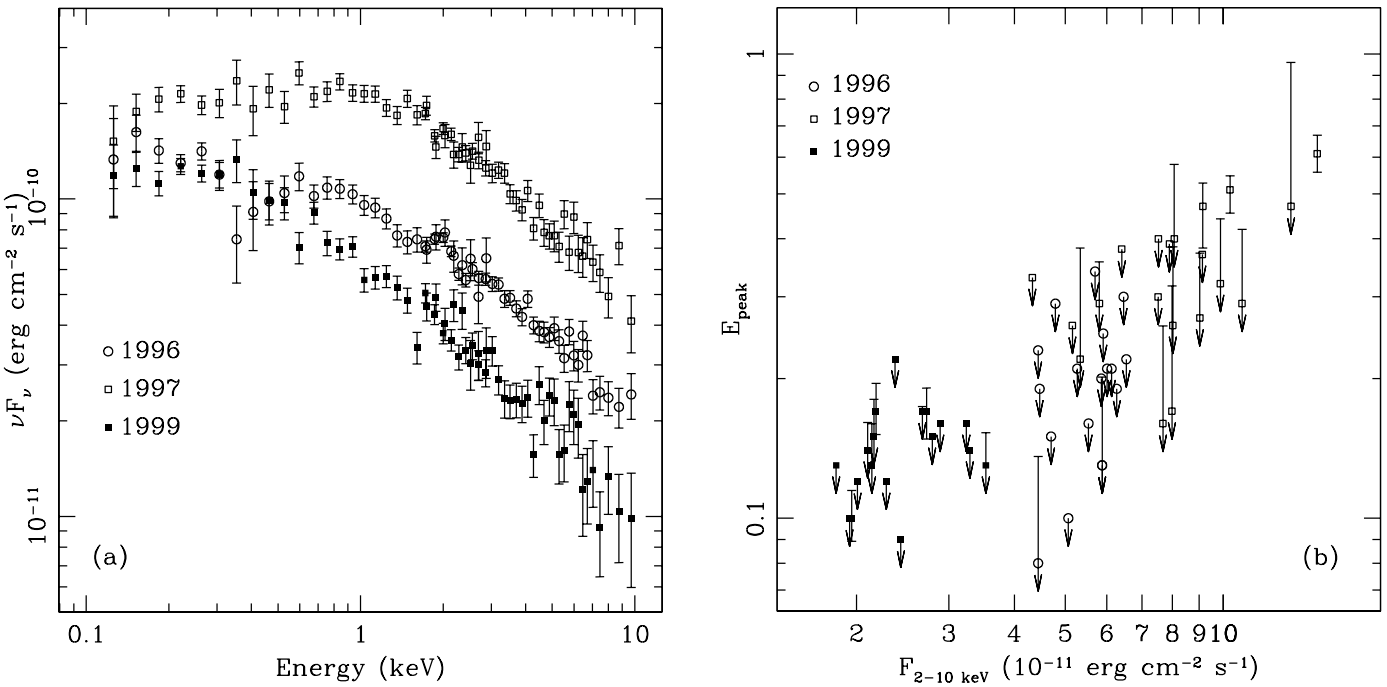


FIG. 9.—(*a*) Deconvolved $\nu F_\nu$ spectrum derived from the segment with maximum flux among each data set, which corresponds to segment 10 of 1996, segment 2 of 1997, and segment 5 of 1999, respectively. (*b*) Peak energies of synchrotron component vs. the 2–10 keV fluxes. A correlation between them is seen, albeit dominated by the upper limits of $E_{\rm peak}$ (see text). These plots demonstrate spectral evolution characterized by the shifts of the synchrotron peak energies.

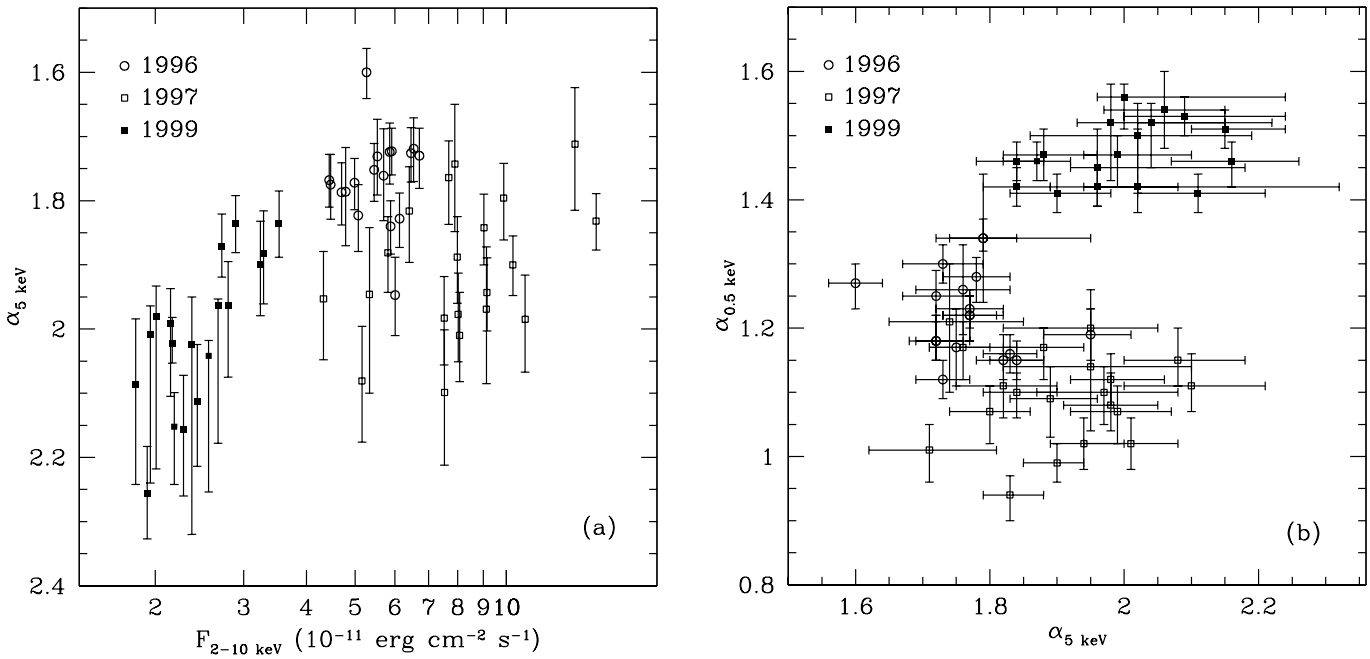


FIG. 10.—(*a*) Spectral index at 5 keV plotted against the 2–10 keV flux. (*b*) Spectral index at 0.5 keV vs. spectral index at 5 keV.

cross-correlation analysis (§ 3.6.4) and the visual inspection of the 1996 light curves (§ 3.1.1 and Fig. 1).

*1997 flare 1*.—Since the increasing phase was not sampled, the spectral behavior is mainly determined by the flare peak and decaying phase, but a clockwise track is clear in both loops, indicating soft lag during this flare. The change in spectral slope is relatively large, with $\Delta\alpha_{0.5\,keV} \simeq 0.2$ and $\alpha_{5\,keV} \simeq 0.3$.

*1997 flare 2*.—The 2–10 keV flux doubled, and the spectral index at 0.5 and 5 keV change by $\Delta\alpha_{0.5\,keV} \simeq 0.2$ and $\Delta\alpha_{5\,keV} \simeq 0.3$, respectively. The loops are quite well defined with a quasi-circular form. The rise and decay phases follow clearly different tracks. It is noticeable that we again find opposite behavior of the loops, but in the opposite sense to the behavior found in the 1996 flare 2. The $\alpha_{0.5\ keV}$-$F$ relation follows a normal clockwise loop, while $\alpha_{5\ keV}$-$F$ follows a counterclockwise loop.

*1997 flare 3*.—This might not be a single flare, so both loops might not have direct meanings. The spectral changes are about 0.2 in both energies.

*1999 flare 1*.—Apart from the second point in the $\alpha_{0.5\ keV}$-$F$ loop, which corresponds to an abrupt rise in the soft energy but not in the hard energies (see Fig. 3), the $\alpha$-$F$ relation might follow clockwise loops in both energies. The spectral index changes little in the rising phase and then softens dramatically by $\Delta\alpha_{5\,keV} \simeq 0.4$ during the decreasing phase, the maximum changes of spectral index obtained in this work. This feature agrees with the flare aspect: a slow rising phase followed by a rapidly decaying phase.

*1999 flare 2*.—The relation of index and flux again follows a clockwise loop, albeit with less significance. The spectral index with large errors changes by $\Delta\alpha_{5\,keV} \simeq 0.2$ during this flare. However, both loops are not well defined because of swing features of the light curve during the peak phase. For example, the visible softening in the third point of the $\Delta\alpha_{5\ keV}$-$F$ loop corresponds to a drop of flux during the rising phase of this flare.

Finally, we notice, in most cases, that the changes of $\alpha_{0.5\ keV}$ are smaller than those of $\alpha_{5\ keV}$ and, in general, that clockwise loops are in agreement with the fact that the DCF/MMD gives soft lags.

## 5. DISCUSSION

In this section we summarize and compare the most important aspects about the variability of PKS 2155−304 that have emerged from this and other works (§ 5.1). The variability of Mrk 421 and Mrk 501 are also compared. The implications of our results are explored on the basis of the internal shock taking place in the jet (§ 5.2).

### 5.1. *Summary and Comparison with Other Observations*

#### 5.1.1. *Power Spectral Density*

Power spectral density or structure function can identify the nature of the variability of a source. The information carried by the PSD has not yet been well explored in blazars. In the X-rays, PSD has been studied recently in some details for the three TeV sources.

The PSDs (§ 3.4) and SFs (§ 3.5) derived in this work with the three *BeppoSAX* data sets indicate that PKS 2155−304 shows red noise variability. The steep power-law slopes (PSD) of ∼2–3 further suggest that the source shows shot-noise variability. PSD or SF of this source was previously studied in the X-ray and optical bands. Tagliaferri et al. (1991) first analyzed the three *EXOSAT* short observations (length of ∼10 hr each). In the 1–6 keV energy band, an average PSD power-law slope of $\alpha \simeq 2.5 \pm 0.2$ was found, which, however, reduced to $\alpha \simeq 1.9 \pm 0.4$ after the removal of the linear trend in the light curves. The SF derived from the *EXOSAT* data was shown in Paltani (1999). Hayashida et al. (1998) derived an average PSD of PKS 2155−304 using four *Ginga* observations (length of about 1–2 days each; light curves were presented in Sembay et al. 1993). The

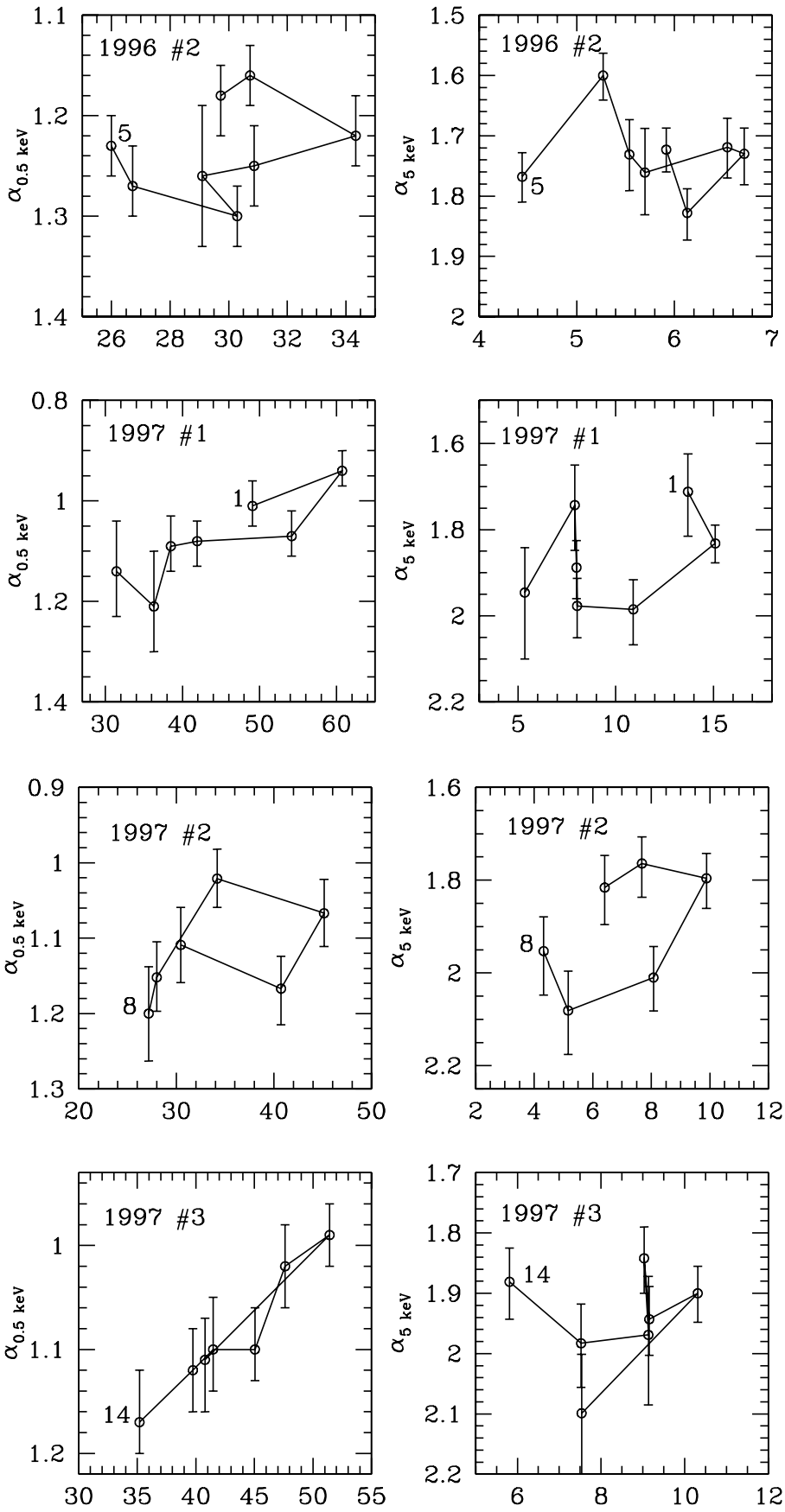


FIG. 11.—Spectral index at 0.5 keV (*left*) and 5 keV (*right*) as a function of the 0.1–2 keV and 2–10 keV flux (in units of $10^{-11}$ ergs cm$^{-2}$ s$^{-1}$) to illustrate the sign of time lags. The starting point of each loop is indicated with the segment number of each observation, and the evolutionary direction follows the connected line.

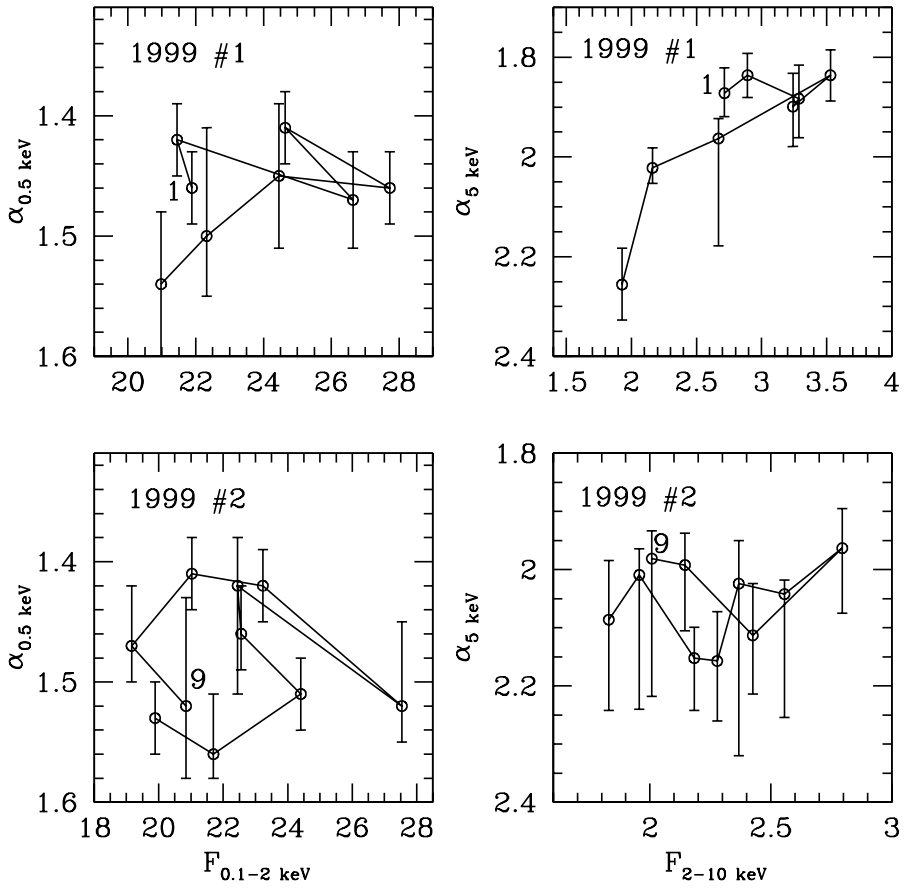


FIG. 11.—*Continued*

PSD slope was $2.83^{+0.35}_{-0.24}$. Very recently, Kataoka et al. (2001) analyzed the *ASCA* and the *RXTE* data sets. They reported steep power-law slopes of ∼2–3. They also reported a break frequency of $(1.2 \pm 0.4) \times 10^{-5}$ Hz for the PSD derived with the about 12 day *RXTE* data set. In the optical, Paltani et al. (1997) studied the short-term variability of PKS 2155−304 and derived the SFs based on the densely sampled 15 night data. They found that the optical PSD (from SFs) was well described by a power-law slope of 2.4. In summary, the slopes of PSDs of PKS 2155−304 obtained by other authors are essentially compatible with those of the present analysis; that is, this source shows the power-law PSD with slopes of ∼2–3 in the studied frequency range.

PSDs of Mrk 421 and Mrk 501 were recently studied by Kataoka et al. (2001) with the *ASCA* and the *RXTE* data sets. These two sources also show power-law PSDs with slopes of ∼2–3. For the long data set, Mrk 421 and Mrk 501 also show a break frequency of $(9.5 \pm 0.1) \times 10^{-6}$ and $(3.0 \pm 0.9) \times 10^{-5}$ Hz, respectively. Cagnoni, Papadakis, & Fruscione (2001) studied the extreme-UV variability of Mrk 421. The extreme-UV PSD is well represented by a power-law slope of $2.14 \pm 0.28$, breaking at ∼3 days.

Finally, we point out that the PSDs of the TeV sources are different from those of Seyfert galaxies and Galactic black hole candidates (GBHCs). The PSDs of the latter can be represented by a power-law model in the high-frequency range, while the slopes are rather distinct from those of the TeV sources. It is noticeable that the TeV sources tend to show steeper slopes ($\alpha \sim 2$–3) than Seyfert galaxies and GBHCs do ($\alpha \sim 1$–2; see, e.g., Hayashida et al. 1998). This difference presumably indicates the different origins and/or sites for the X-ray production. The X-ray emission of Seyfert galaxies and GBHCs is thought to be due to thermal Comptonization of the soft photons (from the accretion disk) by the hot, thermal electrons (from coronae; see, e.g., Nowak et al. 1999; Nandra & Papadakis 2001), while the synchrotron emission from a beamed jet is the most probable origin of the X-rays in the TeV blazars.

#### 5.1.2. *Timescales*

The X-ray observations have revealed that the TeV sources exhibit successive flares. A natural question is whether there is a characteristic timescale related to this phenomenology. However, it is important to first note that most of the observed flares show complicated behaviors, e.g., different durations and amplitude and multiple substructures with shorter timescales.

Timescales of the X-ray variability are important parameters because they carry direct information about the physical processes in the vicinity of the central black holes. The PSD technique is basically used to detect those timescales that can be inferred from the presence of the low- and high-frequency "breaks" or "periodicities" of the PSD. However, because some issues, such as irregularly sampled astronomical data and inefficiently sampled length of the

observations, plague the Fourier-based PSD analysis, the inference of timescales from PSD becomes impossible in most cases. The SF method, partially minimizing these issues, may have the advantage to give an estimate of the timescales. SF analysis (§ 3.5) showed that the X-ray variability of PKS 2155−304 has two common features: a steep slope (∼1.4) at the short timescale range and a turnover[9] at $\tau_{max}$, which is indicative of the timescale characteristic of the durations of the individual flares; $\tau_{max}$ measures the maximum correlated timescale of the system, i.e., whatever the origin and the nature of the variations, the timescale during which "memory" of the variability can be maintained.

It is not yet clear what determines the observed (rising and decay) timescales and the shape of a flare. There are several physical timescales involved, including cooling and acceleration timescales of relativistic electrons, $t_{cool}$ and $t_{acc}$, the electron injection (shock crossing) timescale, $t_{inj}$, and the light crossing timescale, $t_{crs}$. These timescales may play a joint role (see, e.g., Chiaberge & Ghisellini 1999). If $t_{cool}$ is shorter than $t_{crs}$, the variability of the flare is dominated by $t_{crs}$, and the rising and the decaying phase of the observed flare should have symmetric profiles whose timescale $\tau_f$ reflects the size of the emitting region (§ 5.2; eq. [2]). In such a case, we have the relationship of $\tau_{max} = \tau_f = t_{crs}$. This scenario is plausible to apply to the TeV sources in the hard X-ray energy band that corresponds to the shortest $t_{cool}$ range of relativistic electrons responsible for the emission. Within the jet geometry (§ 5.2; eq. [3]), the site of the emitting region can be estimated. This idea is supported by the observed quasi-symmetric profiles of some flares, but this feature is usually broken by unclear factors. However, if the system is observed at the energy where $t_{cool}$ is larger than $t_{crs}$, the flare will show a slower decay phase than the rising phase. In such a case, $\tau_f$ of the rising phase, which is smaller than $\tau_f$ of the decaying phase, reflects the size of the emitting region. These two cases are viable if $t_{inj}$ is smaller than $t_{crs}$. If $t_{inj} > t_{crs}$, a plateau should appear during the flare.

However, the determination of $\tau_{max}$ from an observed light curve is rather ambiguous. Apart from the underlying emission component that may exist, the obvious scenario is that an observed flare can be a superposition of several individual flares. These complexities prevent us from getting the physical meaning of $\tau_{max}$. Moreover, each light curve consists of successive flares that show different amplitude and duration. SF analysis, by definition, is dominated by the flares with larger amplitude and longer duration, and the more rapid shots are suppressed. Therefore, $\tau_{max}$ only carries information on the flares with larger amplitude.

In the literature, $\tau_{max}$ is assumed to be a constant as a common feature of a source (see, e.g., Kataoka et al. 2001). In fact, this statement is oversimplified because it means that the site and the size of the emitting region are constant with time. Of course, we believe that $\tau_{max}$ should be in a limited range, as suggested by our results, which show that $\tau_{max}$ varies by almost an order of magnitude, ranging from $\sim 10^4$ s to about 1 day (§ 3.5; Table 4). This is in agreement with the visible differences of the flare duration between different observations. We also notice similar phenomenology in Mrk 421, observed with *BeppoSAX*; $\tau_{max}$ ranges from $\sim 2 \times 10^4$ to $\sim 7 \times 10^4$ s (Zhang 2000).

At the energies under consideration, $t_{crs} > t_{cool}$ also implies that the symmetric profile of the observed X-ray flares traces the time dependence of the electron acceleration mechanism (modulated by light crossing delays). The importance of the light crossing effects suggests that the manner in which the electrons are accelerated and the density profile of the electrons are both important factors in determining the shape of the flare (Lawson, McHardy, & Marscher 1999). The flare, corresponding to the variation in the number of relativistic (radiating) electrons, could correspond to either the variation in the efficiency of the acceleration of relativistic electrons or the density of electrons that are accelerated. As an example of a reasonable physical situation, Lawson et al. (1999) simulated a flare via synchrotron self-Compton (SSC) emission, caused by a square-shock excitation passing through a spherical emitting region with the electron density and magnetic field falling exponentially with distance from the center. The simulated light curve fits quite reasonably the symmetric X-ray flare of 3C 279 observed with *RXTE*. Thus, the flare can be reproduced with a relatively simple geometry, and the cooling timescales do not dominate the shape of the light curve.

#### 5.1.3. *Time Lags*

The cross-correlation analysis focusing on the "single" flares (§ 3.6) showed that the interband soft lags of PKS 2155−304 differ from flare to flare. The value of the soft lag may relate to the duration of the flare, in the sense that a flare with longer duration may show a larger soft lag. The energy dependence of the soft lags was suggested for the three flares with longer duration (Fig. 8). It is necessary to point out that, given the large uncertainties in the determination of the time lags, these results are still indicative and have yet to be further tested with higher quality data. However, in most cases such uncertainties might be intrinsic to the complicated behaviors of the observed flares themselves rather than to the sampling problems, photon statistics, and the analysis techniques.

It is important to compare our results with others, especially those obtained with other satellites. A long look at PKS 2155−304 with *ASCA* seems to reveal larger soft lags (Tanihata et al. 2001) in two flares. If the correlation between the soft lag and the duration of the flare was real, the results with *ASCA* would be explained because the flares show larger duration. The exception is the third flare that is much more complicated. Observations of Mrk 421 and Mrk 501 with *BeppoSAX* and *ASCA* also showed that the time lags are different from flare to flare. The results for Mrk 421 with *BeppoSAX* and *ASCA* are essentially consistent with each other (Zhang 2000; Takahashi et al. 2000); both the soft and hard lags were found. A hard lag of about 2 hr was reported for Mrk 501 (Tanihata et al. 2001). Energy dependence of time lags has also been reported for Mrk 421 and Mrk 501 (Zhang 2000; Tanihata et al. 2001).

The latest results obtained with *XMM-Newton* are questioning the detection of the time lags with *BeppoSAX* and *ASCA*. Because of the highly eccentric ∼48 hr orbit, uninterrupted data (of one flare) can be obtained. Therefore, it is believed that the results derived from such data are more reliable. Edelson et al. (2001) and Sembay et al. (2002)

[9] Although the presence of this turnover should, in principle, correspond to the low-frequency "knee" of the PSD, our analysis does not show this correspondence, probably because of the limitation of the data (see Appendix C).

reported that no interband time lags exist in two (PKS 2155−304) and three (Mrk 421) data sets observed with *XMM-Newton*. They further proposed that the soft or hard lags detected with *ASCA* and *BeppoSAX* could be biased by the periodic interruption due to the Earth occultation. We, however, notice that there is an important difference between the *XMM-Newton* data and those of *ASCA* and *BeppoSAX*: the available *XMM-Newton* observations did not show flares with large duration comparable to those of *BeppoSAX* and *ASCA*. It is necessary to point out that the *BeppoSAX* and *ASCA* data also showed time lags close to zero. Furthermore, as mentioned in § 3.6, CCFs calculated from more than one flare together may produce spurious zero lag. We have noticed this issue in the long look at Mrk 421 with *BeppoSAX* in 2000 May, which involved several significant flares: the CCF of the entire observation suggested zero lag. However, when each single flare was cross-correlated, different results were derived, and both soft and hard lags were found (Zhang 2000). Variable time lags are physically expected if the parameters of the emitting region change from flare to flare (see § 5.2). Finally, we point out that, because of the complexities of the observed light curves, there exist ambiguities in defining a flare.

#### 5.1.4. *Synchrotron Peak Energies*

Given that $E_{\rm peak}$ is close to the *BeppoSAX* lower energy limit, the present analysis cannot give reliable results about the evolution of $E_{\rm peak}$ of PKS 2155−304. However, an indicative correlation between $E_{\rm peak}$ and the flux (Fig. 9*b*) is still meaningful, indicating that $E_{\rm peak}$ may shift to higher energies with increasing flux.

Such a correlation was found with higher confidence in Mrk 421 and Mrk 501. Fossati et al. (2000b) found that Mrk 421 showed a correlation of $E_{\rm peak} \propto F^{0.55\pm0.05}$, and Tavecchio et al. (2001) reported that Mrk 501 showed a relation of $E_{\rm peak} \propto F^{\sim 2}$. The significant difference of the slopes was interpreted by Tavecchio et al. (2001) with the dependence of the slope of the $E_{\rm peak}$-$F$ relation on the position of the peak being steeper when the peak is at higher energies. The reason for the change of the slope is that the flux is evaluated in a limited energy band. When $E_{\rm peak}$ is located at the lower energy boundary of the studied energy band, a small shift of $E_{\rm peak}$ can cause a large change in the flux, and hence the slope of the $E_{\rm peak}$-$F$ relation will be smaller than 1. Once $E_{\rm peak}$ moves toward the upper limit of the studied energy band, the increase of the flux is less rapid, and hence the $E_{\rm peak}$-$F$ relation will be steeper. This phenomenology has also been found in Mrk 421 itself: the 2000 *BeppoSAX* data (in a very high state; G. Fossati et al. 2002, in preparation) may show a steeper $E_{\rm peak}$-$F$ relation than that found in the 1997 and 1998 *BeppoSAX* data (Fossati et al. 2000b).

#### 5.1.5. *Spectral Variability*

Our analysis has revealed that PKS 2155−304 showed complex X-ray spectral variability, with different variability modes detected. Our results suggest the following basic facts: (1) On a timescale of hours (for each observation), there is no correlation of the spectral slopes and the fluxes (Fig. 10*a*). If the rising and decaying phase of each flare follows different tracks on the $\alpha$-$F$ plane, there will be large scatter for the correlation between them. Moreover, there might be no such correlation over long timescales (from epoch to epoch). This phenomenology was also found in Mrk 421 with the *XMM-Newton* observations (Sembay et al. 2002). (2) It seems that spectral indices in the soft and hard X-rays do not correlate with each other (Fig. 10*b*). This could be interpreted if there were time delay of the spectral changes at different energies. (3) Our analysis indicates that the spectral curvature (from soft- to hard X-rays) of the 1997 data is larger than the curvature of the 1996 and 1999 spectra. This can be explained if $E_{\rm peak}$ of the former is located in the soft X-rays, while $E_{\rm peak}$ of the latter may move down to the UV band, from which smaller spectral curvature is expected in the X-ray band. Note, however, that Sembay et al. (1993) found a tight correlation between the spectral index in the 3.8–17.9 keV and 1.7–3.8 keV ranges with *Ginga* observations, and the higher energy index is systematically steeper by $\Delta\alpha \sim 0.2$, indicating that the degree of curvature of the spectrum is constant. The two behaviors are not in contradiction because the results of Sembay et al. (1993) do not cover the soft-energy part of spectrum.

We have entered into details to study the $\alpha$-$F$ relation of each flare of PKS 2155−304 (Figs. 4 and 11). With this technique, Sembay et al. (1993) found both the soft and hard lag behaviors in this source. Kataoka et al. (2000) reported a clockwise loop with *ASCA* data. We further found more complicated evidence that two flares track opposite directions in the soft and hard bands, indicating changes of the sign of the time lags from the soft to hard-energy band.

On the $\alpha$-$F$ plane, Mrk 421 showed a counterclockwise loop during a large flare detected by *BeppoSAX*, indicating a hard lag (Fossati et al. 2000b; Zhang 2002).

### 5.2. *Implications for the Dynamics and the Structure of the Jet*

Because of rapid cooling, relativistic electrons responsible for the X-ray emission of the TeV blazars must be repeatedly accelerated (injected) in order to account for successive flares. It is now believed that relativistic electrons are most likely accelerated at shock fronts taking place in the jets. Therefore, the rich phenomenology of the X-ray variability of PKS 2155−304 that emerged from this work, in particular, the characteristic timescale (if any; we identify it as the half-duration of the flare), time lags, peak energies of synchrotron component, and spectral variability, can give important clues on the dynamics and the structure of the jet and its central engine.

Two kinds of shocks have been proposed: internal shocks versus external shocks. The basic difference between them is the site and the way shocks are formed in blazar jets. Both have been extensively applied to gamma-ray burst (GRB) models.

In the scenario of an external shock, the shocks are formed when the relativistic plasma ejected from the central engine sweeps up material from the surrounding medium, where the jet plasma decelerates and its bulk kinetic energy is converted into nonthermal particle energy (see, e.g., Dermer & Chiang 1998).

The idea of internal shock was first proposed to explain some features of the optical jets in M87 (Rees 1978). It was applied to GRB modeling and reconsidered in blazar jets (see, e.g., Ghisellini 2001; Spada et al. 2001), inspired by the close similarities between them. The key idea of this scenario is to assume that the central engine of a blazar is working in an intermittent rather than a continuous way to expel discrete shells of plasma with slightly varying velocities. The

shock will be formed because of a collision when a later faster shell catches up to an earlier slower one. The dissipation of bulk kinetic energy carried by the shells during the shock is used to accelerate particles and generate the magnetic field, from which the radiation is produced by synchrotron and inverse Compton mechanisms.

The observed large amplitude and rapid variability of blazars, particularly the recurrent flares, must be accounted for by a non–steady state pulse (jet) model. The internal shock model can be thought to be the simplest way, in which a series of shell-shell collisions can naturally produce successive flares. In this scenario there should be a "typical" timescale (at least for the first collisions) related to the initial time interval between the two colliding shells and their widths. Inhomogeneities within the shells and smaller scale instabilities can cause variability on shorter timescales to account for small amplitude flickers superimposed on the global trend of the flare. Extremely rapid variability could be due to shocks where the width of the shock is smaller than the width of the jet. There are still other points in favor of the internal shock model (see, e.g., Ghisellini 2001).

Relativistic electrons in the jets of the TeV sources are thought to be accelerated to the maximum energies. The first collisions of the shells have the most efficient energy conversion. Therefore, for simplicity, it is reasonable to assume that an X-ray flare of the TeV sources is produced during the first collision of two shells that have never collided with other shells before, while the more realistic situation is that the central engine would produce a series of shells involving multiple collisions to produce multiple flares.

We assume that the two relativistic shells have bulk Lorentz factors $\Gamma_1$ and $\Gamma_2$ ($\Gamma_2 > \Gamma_1$) and that the initial time interval between them at their departure from the central source is $t_0$. The shell width is initially of the same order as the initial shell-shell separation. The expected distance at which these two shells collide is

$$R \simeq \frac{2a^2}{a^2-1}\Gamma^2 c t_0 \ , \tag{1}$$

where $a = \Gamma_2/\Gamma_1 > 1$ is the ratio of the bulk Lorentz factor of the two shells and $\Gamma$ is the bulk Lorentz factor of the merged shell that is usually identified as the emitting region (blob).

The emitting region is assumed to be a "one-zone" homogeneous spherical blob with radius $r/2$ tangled with magnetic field $B$, moving at relativistic velocity $\beta c$ at a small angle $\theta$ with respect to the line of sight. The bulk Lorentz factor of the blob is described as $\Gamma = (1-\beta^2)^{-1/2}$, and relativistic effects are described by the Doppler factor $\delta = \Gamma^{-1}(1-\beta\cos\theta)^{-1}$. If $\Gamma \gg 1$, the open angle of the jet $\theta$ is approximately equal to $1/\Gamma \simeq 1/\delta$. The blob is filled with "cold" electrons that are being accelerated and, in turn, suffering cooling to produce the emission we are observing.

If one assumes that $t_{\rm crs}$ dominates the system (this condition is thought to be valid in the X-rays of the TeV sources), $\tau_{\rm crs}$ can be observationally identified as $\tau_{\rm max}$ inferred from the SF. Therefore, $\tau_{\rm max}$ gives a constraint on the size of the emitting region

$$r \simeq \Gamma c \tau_{\rm max} \ . \tag{2}$$

If $\Gamma \sim 10$ is assumed, the inferred $\tau_{\rm max}$ (Table 4) suggests that the size of the emitting blob is $\sim 3\times10^{15}$ and $\sim 2\times10^{16}$ cm for the 1997 and 1996/1999 observations, respectively. With the jet geometry, this in turn constrains the distance (from the central engine) where the acceleration and emission takes place,

$$R_e = \frac{r}{\sin\theta} \simeq \frac{r}{\theta} \simeq r\Gamma \simeq \Gamma^2 c\tau_{\rm max} \ . \tag{3}$$

It is reasonable to assume that the emission takes place just after the collision, i.e., $R_e \simeq R$; then we have

$$\tau_{\rm max} \simeq \frac{2a^2}{a^2-1} t_0 \ . \tag{4}$$

Thus, $\tau_{\rm max}$ is a measurement of the initial time interval of the two shells ejected from the central engine if $a$ is not too small, which is also constrained by the efficiency of the energy dissipation. In general, if $a \simeq 2$, then $\tau_{\rm max}$ is between 2 and 3 times $t_0$.

The minimum value of $t_0$ is constrained by the light crossing time across the central source. For a black hole of $M = 10^9\ M_\odot$, this timescale is $\sim 10^4$ s. Therefore, the initial time intervals of the shell pairs to produce the X-ray flares in 1997 are comparable to the minimum timescale constrained by the central engine. The flare durations of 1997 may represent the shortest timescales that can ever be detected in PKS 2155−304.

The acceleration mechanism remains open. In this work the widely discussed diffusive shock acceleration (see, e.g., Drury 1983; Blandford & Eichler 1987) is assumed to be the mechanism responsible for electron acceleration in blazar jets. In the comoving frame, the diffusive shock acceleration timescale $t'_{\rm acc}(\gamma)$ of a relativistic electron with energy $\gamma m_e c^2$ is approximated (see, e.g., Kusunose, Takahara, & Li 2000) as

$$t'_{\rm acc}(\gamma) = \frac{20\lambda(\gamma)c}{3u_s^2} \sim 3.79\times10^{-7}\xi B^{-1}\gamma \ {\rm s} \ , \tag{5}$$

where $\gamma$ is the Lorentz factor of the electron, $m_e$ the electron mass, $c$ the light speed, $u_s \approx c$ the speed of the relativistic shock, and $\lambda(\gamma) = \gamma m_e c^2 \xi/(eB)$ the mean free path assumed to be proportional to the electron Larmor radius, with $\xi$ described as the acceleration parameter. $B$ is the magnetic field in gauss.

In the case of TeV sources, X-ray emission is primarily due to synchrotron radiation. In the comoving frame, the corresponding synchrotron cooling timescale of a relativistic electron with energy $\gamma m_e c^2$, $t'_{\rm cool}(\gamma)$, is (see, e.g., Rybicki & Lightman 1979)

$$t'_{\rm cool}(\gamma) = \frac{6\pi m_e c}{\sigma_T} B^{-2}\gamma^{-1} \sim 7.74\times10^8 B^{-2}\gamma^{-1} \ {\rm s} \ . \tag{6}$$

One can see from the above two equations that $t'_{\rm acc}$ and $t'_{\rm cool}$ depend on electron energy, in the sense that lower energy electrons can be accelerated to the radiative window in shorter time but cool during a longer time. It is convenient to express $t'_{\rm acc}(\gamma)$ and $t'_{\rm cool}(\gamma)$ in terms of the observed photon energy because the typical synchrotron emission frequency, averaged over pitch angles, of an electron with energy $\gamma m_e c^2$ peaks at photon energy $\nu \sim 3.73\times10^6 B\gamma^2$ Hz. In the observer's frame, we have

$$t_{\rm acc}(E) = 9.65\times10^{-2}(1+z)^{3/2}\xi B^{-3/2}\delta^{-3/2}E^{1/2} \ {\rm s} \ , \tag{7}$$

$$t_{\rm cool}(E) = 3.04\times10^3(1+z)^{1/2}B^{-3/2}\delta^{-1/2}E^{-1/2} \ {\rm s} \ , \tag{8}$$

where $E$ is the observed photon energy in units of keV for the convenience of X-ray studies. It is obvious that $t_{\rm cool}$ and $t_{\rm acc}$ have the "same" degree of dependence on the photon energies (square root of the energy) but in the opposite way; i.e., the lower energy photons have shorter accelerating but longer cooling timescales than the higher energy photons do. It is then reasonable to assume that the soft and hard lags of the response of the low-energy X-ray variations compared with those of the high-energy X-ray ones reflect the difference of $t_{\rm cool}$ and $t_{\rm acc}$ of relativistic electrons responsible for the emission in the studied energy bands, respectively. If $t_{\rm acc} \sim t_{\rm cool}$, the observed hard lag is expected to be $\tau_{\rm hard} = t_{\rm acc}(E_h) - t_{\rm acc}(E_l)$, from which physical parameters of the emitting blob can be constrained,

$$B\delta\xi^{-2/3} = 0.21(1+z)E_h^{1/3}\left[\frac{1-(E_l/E_h)^{1/2}}{\tau_{\rm hard}}\right]^{2/3} \ {\rm G}\ , \quad (9)$$

where $E_l$ and $E_h$ refer to the low- and high-energy bands in units of keV, respectively. Similarly, if $t_{\rm acc} \ll t_{\rm cool}$, the observed soft lag is expected to be $\tau_{\rm soft} = t_{\rm cool}(E_l) - t_{\rm cool}(E_h)$, from which physical parameters of the emitting blob can be constrained,

$$B\delta^{1/3} = 209.91\left(\frac{1+z}{E_l}\right)^{1/3}\left[\frac{1-(E_l/E_h)^{1/2}}{\tau_{\rm soft}}\right]^{2/3} \ {\rm G}\ . \quad (10)$$

Note that, in practice, $E_l$ and $E_h$ are taken as the logarithmic mean energies in the corresponding energy bands used in the cross-correlation analysis, taking into account power-law decrease of the X-ray flux with increasing energy in the TeV sources. It is interesting to note that $t_{\rm acc}$ and $t_{\rm cool}$ have the same dependence on the magnetic field $B$; the ratio of $t_{\rm acc}$ to $t_{\rm cool}$ is thus independent of $B$:

$$\frac{t_{\rm acc}(E)}{t_{\rm cool}(E)} = 3.17\times10^{-5}(1+z)\xi\delta^{-1}E = 0.32(1+z)\xi_5\delta_1^{-1}E\ , \quad (11)$$

where $\xi_5$ and $\delta_1$ are in units of $10^5$ and 10, respectively.

Since $\delta$ is thought to be on the order of ~10–25, one can see that $\xi$ is the key parameter to modulate the observed behavior of the variability; i.e., the observed interband relationship of a flare depends on not only the value of $t_{\rm acc}/t_{\rm cool}$ but also on its energy dependence. The value of $\xi$ is poorly known, but changes in $\xi$ provide clues on changes in the parameters of shock formation and acceleration. There are three different behaviors expected for an observed energy range: (1) If $t_{\rm acc} \ll t_{\rm cool}$ across the studied energy band, which corresponds to instantaneous injection of radiating electrons, the cooling process dominates the system, and information on the acceleration is suppressed by cooling. Then information about the emission propagates from higher to lower energy, higher energy photons will lead lower energy ones, and a clockwise loop of spectral index against the flux will be observed; this corresponds to the soft lag pattern (§§ 3.6 and 4.2.2). (2) In contrast, if $t_{\rm acc}$ is comparable to $t_{\rm cool}$ under the considered energy range, the acceleration process dominates the system, information about the emission propagates from lower to higher energy, higher energy photons will lag lower energy ones, and a counterclockwise loop of spectral index against flux will be observed; this corresponds to the hard lag behavior. Therefore, information about particle acceleration is observable only if the source is observed at energies closer to the maximum (characteristic) synchrotron radiating energy, $E_{\rm max}$, where $t_{\rm acc} = t_{\rm cool}$ (Kirk, Rieger, & Mastichiadis 1998), indicating a relatively low rate of acceleration. The value of $E_{\rm max}$ emitted by the maximum energy of electrons ($\gamma_{\rm max}$), which can be accelerated, is determined by the balance between acceleration and cooling (see, e.g., Kirk et al. 1998). (3) The most interesting behavior may occur if $E_{\rm max}$, where $t_{\rm cool} = t_{\rm acc}$, is inside the high-energy end of the considered energy band. $E_{\rm max}$ ($=3.7\times10^6\delta B\gamma_{\rm max}^2$ Hz) can be estimated to be a few keV with the general parameter ranges ($\gamma_{\rm max} \sim 10^5$, $B \sim 0.1$ G, and $\delta \sim 10$) of the emitting region inferred from the SEDs of the source (see, e.g., Kino, Takahara, & Kusunose 2002). The observed time lag will gradually evolve from a soft lag to a hard lag at an energy ($E_{\rm app}$) where $t_{\rm acc}$ approaches $t_{\rm cool}$, say, $t_{\rm acc} \sim 0.9t_{\rm cool}$. Equation (11) implies that $E_{\rm app}$ is ~2.5 keV if $\xi_5 = 1$, $\delta_1 = 1$, and $z = 0.116$ are assumed. This is an alternative and the simplest explanation for the behavior of the 1997 flare 2, which shows a soft and hard lag in the soft and hard-energy band, respectively (see Fig. 11). This is the first time that the interplay between acceleration and cooling time is simultaneously observed through the behavior that soft lags evolve to hard lags from low to high energies. $E_{\rm max}$ determines the position of the switching point from the soft to hard lag. This phenomenology demonstrates the importance of $t_{\rm acc}$ being energy-dependent. However, the current time-dependent models involving acceleration have not yet considered this effect. For the convenience of numerical simulations, $t_{\rm acc}$ is assumed to be energy-independent (see, e.g., Kirk et al. 1998; Kusunose et al. 2000).

However, the opposite behavior observed in 1996 flare 2 cannot be accounted for by this interpretation but could be explained with a two-component model, of which one component (lower energy) dominates at soft energies and one (higher energy) dominates at hard energies. If the former comes first, the hard lag in the soft energies and the soft lag in the hard energies are expected if the latter is dominated by the soft lag. It seems that this idea is consistent with the fact that $\sigma_{\rm rms}^2$ in the 0.1–0.5 keV band may be larger than that in the 0.5–2 keV band (see § 3.2 and Table 2) as long as the synchrotron peak energy of the first (lower energy) componentis smaller than that of the second (higher energy) component.

The internal energy dissipated from the bulk kinetic energy of the two colliding shells is shared among protons, electrons, and the magnetic field. In the case of the magnetic field generated only from the energy dissipation in each collision and neglecting any seed magnetic field that can be amplified by shock compression, the value of magnetic field $B$ strongly anticorrelates with collision distance $R$ approximately as (Spada et al. 2001)

$$B \propto R^{-3/2}\ . \quad (12)$$

This relation should be the case for the TeV sources because the X-ray flares are thought to be produced from the first collisions of the shells that have never collided before (i.e., shells without internal energy before collisions).

Equation (10) gives the following relation:

$$B\Gamma^{1/3} \propto \tau_{\rm lag}^{-2/3}\ . \quad (13)$$

Then we have

$$\tau_{\rm lag} \propto \Gamma^{-1/2} R^{9/4} . \quad (14)$$

Substituting $R$ (i.e., $R_e$) in equation (3), we can get

$$\tau_{\rm lag} \propto \Gamma^4 \tau_{\rm max}^{9/4} . \quad (15)$$

One can see that the soft lag increases steeply with $\tau_{\rm max}$ since the change of $\Gamma$ is very small. Therefore, the changes of soft lags from flare to flare inferred from the cross-correlation analysis are in qualitative agreement with this prediction, which suggests that smaller soft lags are related to the flares with shorter duration.

In the simplest "one-zone" SSC model, the electron distribution is described by a broken power law with cutoff energy $\gamma_{\rm max}$ either on the basis of the pure phenomenology or on the basis of the kinetic equation; $\gamma_{\rm max}$ is determined by a detailed balance between acceleration and cooling. The break energy $\gamma_{\rm break}$ is observationally recognized as the $E_{\rm peak}$ through the relation $E_{\rm peak} \propto \delta B \gamma_{\rm break}^2$. Therefore, an increase of $E_{\rm peak}$ from a low state (similar to that observed in 1996 and 1999) to a high state (like that of 1997) can be ascribed to an increase of $\gamma_{\rm break}$, $B$, and $\delta$, of which $\gamma_{\rm break}$ is the key parameter regulating the observed variability.

The simulation by Spada et al. (2001) showed that the values of $E_{\rm peak}$ of synchrotron radiation pulses decrease with the increasing collision distance along the jet (see their Fig. 5). The values of $E_{\rm peak}$ at each distance have been obtained by averaging over all of the collisions occurring at that distance. This is in agreement with our findings that $E_{\rm peak}$ in 1997 is higher because of smaller collision distance (i.e., smaller duration of the flares). Note that the parameters of their simulations are adopted typically for flat-spectrum radio quasars like 3C 279, which has very low peak energy with respect to the TeV sources.

The variations of $\gamma_{\rm break}$ ($E_{\rm peak}$) from flare to flare can be explained by the variations in the structure of the shock (the key parameter is $t_{\rm acc}$), which may depend on the colliding distance of the two shells. The initial separation time $t_0$ of the two shells is the most critical parameter that determines the distance at which the collision happens.

Finally, it is necessary to point out that our interpretation for the complex variability patterns is based on the simplest scenario, i.e., the interplay between acceleration and cooling processes. It is worth noting that other possible effects may influence the observed flux behavior. The X-ray emission in PKS 2155−304 (and other TeV sources) originates in the fast cooling regime of the relativistic electron energy distribution, which causes the fast changing of the SED. Therefore, the light curve (flare) at a fixed frequency corresponds to the different parts of the SED of the source (as in the case of GRBs; see, e.g., Sari et al. 1998). This uncertainty may change the relation of light curves at different energies and the evolution of spectral indices with the flux. Furthermore, the flare's profiles depend on such parameters as shock/dissipation lifetime, electron injection time profile, adiabaticity, and the half-opening angle of the jet (Sikora et al. 2001). In the context of the radiative hydromagnetic shocks, the interplay between the cooling and the compression may also play an important role. Granot & Königl (2001) showed that when synchrotron radiation dominates the cooling, this effect becomes more pronounced on account of the feedback effect between the field amplification and the emission process: a strong magnetic field increases the emissivity, which in turn induces a larger compression that further amplifies the field. However, the determination of a specific mechanism responsible for a flare pattern (e.g., energy-dependent time lags and local spectral evolution) requires the comparison between the flare behavior and the numerical simulation of the radiative shocks. We also note that the theoretical study of the radiative shock structure and evolution in the jets of blazars has so far been little developed.

## 6. CONCLUSIONS

*BeppoSAX* continuously monitored PKS 2155−304 for about 2 days in November of 1996, 1997, and 1999. We have studied and interpreted the joint behavior of temporal and spectral evolution in the X-ray range. During these observations, the source was in different states of brightness and showed a variety of variability behavior. This provides us with rich information about this source, which in turn reveals some interesting clues on the physical processes operating in jets. We summarize our main results as follows:

1. The amplitude of variability is larger and the doubling timescale shorter at higher energy. Neither quantity correlates with the brightness of the source, and complex behaviors are detected.
2. The PSDs (and the SFs) are characterized by a featureless red noise steep power law of $f^{-2\sim-3}$, indicating that the variability of the source can be ascribed to the shot noise.
3. The SFs show evidence for the presence of a "turnover" characteristic of the timescales of the repeated flares, i.e., the average value of the half-duration of the flares. More importantly, our analysis revealed that this timescale changes over a factor of a few, which could determine the overall behavior of the flares.
4. Detailed cross-correlation analyses revealed that the soft X-ray photons lag the hard ones. Interestingly, the values of soft lags seem to correlate with the duration of the flares.
5. Time-resolved spectral fits with a curved model suggest that the peak position of synchrotron emission moves to higher energy with increasing flux.
6. Spectral changes are complicated without any clear correlations of spectral slope versus flux and between spectral slopes at different energies.
7. The tracks between the spectral indices and the fluxes showed a variety of modes. The changes of the sign of the time lags from the soft to hard energy were found in two flares. The other flares show only soft lags across the studied energy band.

As a possible interpretation of the observed variability of PKS 2155−304, the internal shock was discussed in line with the homogeneous synchrotron cooling mechanism. It turns out that our analyses are qualitatively consistent with the predictions of such a scenario:

1. The (half-)duration of the flare indicates the initial time interval of the two shells ejected from the central engine to produce the flare. This time interval determines the distance at which the collision of the shells takes place, which in turn may fix the structure of the shocks and physical parameters of the emitting region.
2. The shot-noise mode of the variability indicates recurrent flares. A series of shells should be intermittently ejected in order to form successive flares.

3. The changes of the durations, the soft lags, and synchrotron peaks from flare to flare are fully consistent with predictions of the internal shocks if they form at different distances.

4. The discovery of the interband time lags switching from the soft to hard lag during the 1997 flare 2 emphasizes the importance of electron acceleration being energy-dependent.

5. The variability behavior of the 1996 flare 2 suggests that the flare may consist of more than one emission component with different spectral energy distribution.

In the scenario of the internal shock, the initial conditions (mainly the time interval) of the two shells that collide to produce the flare may determine at the first order of approximation the main properties of the observed flares in PKS 2155−304.

Part of this work was conducted at SISSA during the Ph. D. project of Y. H. Z. The anonymous referee is thanked for constructive comments. We greatly thank the *BeppoSAX* Science Data Center for providing the standard event files archive. We acknowledge the Italian MUIR for financial support.

## APPENDIX A

## EXCESS VARIANCE

The normalized excess variance $\sigma_{\rm rms}^2$ is defined as

$$\sigma_{\rm rms}^2 = \frac{1}{N\bar{x}^2}\sum_{i=1}^{N}\left[(x_i-\bar{x})^2-\sigma_i^2\right], \tag{A1}$$

where $x_i$, with quoted error $\sigma_i$, is the count rate and $\bar{x}$ is the unweighted arithmetic mean count rate over $N$ points of a light curve. One can see that $\sigma_{\rm rms}^2$ is defined as the difference between total (standard) variance, $\sigma_{\rm total}^2 = (1/N)\sum_{i=1}^{N}(x_i-\bar{x})^2$, and noise variance, $\sigma_{\rm noise}^2 = (1/N)\sum_{i=1}^{N}\sigma_i^2$, which in turn is normalized by $\bar{x}^2$ to compare $\sigma_{\rm rms}^2$ between different light curves. The error on $\sigma_{\rm rms}^2$ is estimated by $s_D/(\bar{x}^2\sqrt{N})$ (Turner et al. 1999), where

$$s_D^2 = \frac{1}{N-1}\sum_{i=1}^{N}\left\{\left[(x_i-\bar{x})^2-\sigma_i^2\right]-\sigma_{\rm rms}^2\bar{x}^2\right\}^2, \tag{A2}$$

i.e., the variance of the quantity $(x_i-\bar{x})^2-\sigma_i^2$. The fractional variability parameter $F_{\rm var}$ used in Zhang et al. (1999) is the square root of the excess variance: $F_{\rm var} = (\sigma_{\rm rms}^2)^{1/2}$.

Power spectral density analysis of PKS 2155−304 performed in § 3.4 has revealed larger amplitude variability at lower frequencies than at higher frequencies. The PSD can been parameterized by a power-law form (see also Appendix B)

$$P(f) = Cf^{-\alpha}, \tag{A3}$$

where $C$ is the normalized amplitude of the PSD and $\alpha$ is the slope of PSD. The excess variance $\sigma_{\rm rms}^2$ can be obtained by integrating the PSD

$$\sigma_{\rm rms}^2 = 2C\int_{f_1}^{f_2} P(f)df \tag{A4}$$

$$= \frac{2C}{1-\alpha}\left(f_2^{1-\alpha}-f_1^{1-\alpha}\right) \tag{A5}$$

$$= \frac{2C}{\alpha-1}\left[T^{\alpha-1}-\left(\frac{\Delta t}{2}\right)^{\alpha-1}\right]. \tag{A6}$$

The $\sigma_{\rm rms}^2$ will thus depend on the exact range of temporal frequencies, i.e., observing length ($T = 1/f_1$) and binning [$\Delta t = 1/(2f_2)$] of the light curve. Different sampling pattern can be corrected by normalizing variance to the same frequency range.

If $T \gg \Delta t$, we have

$$\sigma_{\rm rms}^2 \propto T^{\alpha-1} \tag{A7}$$

for $\alpha > 1$ and no changes of $\alpha$ across the frequency interval $[1/T, 1/(2\Delta t)]$.

The $\sigma_{\rm rms}^2$ of 1996 and 1997 is normalized to the observing length of 1999, the longest one, and $\alpha \sim 2.5$ derived in § 3.4 is applied. The amplified factor is ~1.2 and ~2.5 for 1996 and 1997, respectively. However, the real values may decrease significantly if there is a knee or break of PSD at a frequency larger than $1/T$, especially for 1997 since a relatively short characteristic timescale is suggested by its SFs.

The second important effect on the observed variance is different binning. For the same length of observation, the variance from the smaller bin size should be no smaller than those from the larger bin size since larger binning will tend to reduce the observed variance by integrating out high-frequency power. However, in fact, the situation is not always like this. As seen from Table 2, $\sigma^2_{\rm rms}$ values derived from the 600 s bin are significantly smaller than those derived from 5670 s bin in some cases. We consider this effect as being due to lower signal-to-noise ratios associated with the 600 s bin, and particularly, in some bins noise variance will be larger than the count rate variance, which inevitably reduces source variance. Therefore, smaller binning has a strong tendency to reduce the observed variance by integrating negative high-frequency power caused by insufficient signal-to-noise ratios. When the signal-to-noise ratio is high enough, this will not happen. As seen from Table 2, $\sigma^2_{\rm rms}$ values derived from the 600 s bin are indeed larger than those derived from the 5670 s bin in the case of the 0.5–2 keV and 2–4 keV band of 1997, while the statistics are not significant.

Quantifying the effects caused by binning, signal-to-noise ratio, and gaps together would be analytically impossible and needs detailed simulations. However, the observed excess variance estimated from light curves binned over 5670 s will not be affected by these uncertainties, and the only uncertainty is the observing length. This is because the 5670 s binned light curves are evenly sampled, and the signal-to-noise ratio is high. There are still uncertainties caused by the low exposure time of the LECS, but it may not be significant.

Therefore, in § 3.2 we use $\sigma^2_{\rm rms}$ derived from 5670 s binned light curves to discuss the energy and intensity dependence of amplitude of variability.

## APPENDIX B

## POWER SPECTRAL DENSITY

The NPSD at frequency $f_k$ is defined as

$$P(f_k) = \frac{\left[c^2(f_k) + s^2(f_k) - \sigma^2_{\rm noise}/N\right]T}{\bar{x}^2} , \tag{B1}$$

$$c(f_k) = \frac{1}{N}\sum_{i=1}^{N} x_i \cos(2\pi f_k t_i) , \tag{B2}$$

$$s(f_k) = \frac{1}{N}\sum_{i=1}^{N} x_i \sin(2\pi f_k t_i) , \tag{B3}$$

where $x_i$ is the count rate at time $t_i = i\Delta t$ ($i = 1, 2, \ldots, N$ and $\Delta t$ is the binning size), $\bar{x}$ the unweighted arithmetic mean count rate, and $T$ the observing length; $c(f_k)$ and $s(f_k)$ ($f_k = k/T$ is the Fourier frequency and $k = 1, 2, \ldots, N/2$) represent the finite cosine and sine components, respectively, of Fourier transform of a light curve. The power due to the white noise $\sigma^2_{\rm noise}$ is subtracted. With this definition, the integration of the source power over the positive frequencies yields half of the excess variance of the same light curve (see eq. [A4]).

A "typical" PSD is characterized by a cutoff frequency $f_{\rm max}$ at high frequency and a break frequency $f_{\rm min}$ at low frequency (to avoid divergence of $\sigma^2_{\rm rms}$). The range between $f_{\rm min}$ and $f_{\rm max}$ is linked by a power-law curve, i.e., $P(f) \propto f^{-\alpha}$, and $\alpha$ depends on the nature of the intrinsic variation of a source (e.g., flicker noise, shot noise).

## APPENDIX C

## STRUCTURE FUNCTION

Simonetti, Cordes, & Heeschen (1985) first introduced the concept of structure function into the field of astronomy. The first-order SF of a time series $x(t)$ at a timescale $\tau$ is defined as

$$\mathrm{SF}(\tau) = \frac{1}{n}\sum \left[x(t+\tau) - x(t)\right]^2 . \tag{C1}$$

In fact, SF($\tau$) as a function of timescale $\tau$ is a measurement of the mean squared flux differences, $x(t+\tau) - x(t)$, of $N$ pairs with the same time separation $\tau$. For an unevenly sampled $x(t)$, $n$ is the number of pairs over an interval of $\tau - \Delta\tau/2 < \tau < \tau + \Delta\tau/2$ for a specific binning pattern $\Delta\tau$ (equally or logarithmically binned). The errors on SF($\tau$) are calculated by the standard deviation of squared flux differences of $n$ pairs in each bin (but see Simonetti et al. 1985 and Cagnoni et al. 2000 for the caveats of using such errors).

A "typical" SF($\tau$) is characterized by the minimum and maximum correlation timescales, $\tau_{\rm min}$ and $\tau_{\rm max}$, and a power-law curve between them, i.e., $\mathrm{SF}(\tau) \propto \tau^{\beta}$. The same as PSD, $\beta$ depends on the variability nature of a source. SF is related with the standard variance and autocorrelation function of the light curve as

$$\mathrm{SF}(\tau) = 2\left[\sigma^2_{\rm total} - \mathrm{ACF}(\tau)\right] . \tag{C2}$$

SF($\tau$) flattens below $\tau_{\rm min}$ and above $\tau_{\rm max}$, approximated as $2\sigma^2_{\rm noise}$ and $2\sigma^2_{\rm total}$, respectively.

SF gives information similar to PSD. There are simple correspondences between the parameters derived from SF and PSD:

$$f_{\rm min} = \frac{1}{\tau_{\rm max}} , \tag{C3}$$

$$f_{\rm max} = \frac{1}{\tau_{\rm min}} , \tag{C4}$$

$$\alpha = \beta + 1 . \tag{C5}$$

However, this relation is valid only in the limit $T \to \infty$ and $\Delta t \to 0$; this condition definitely requires long enough observing length and small enough temporal resolution with high signal-to-noise ratio. In fact, since the PSD is strongly limited to a small frequency range $[1/T, 1/(2\Delta t)]$, these relationships do not hold any more.

## REFERENCES


Blandford, R., & Eichler, D. 1987, Phys. Rep., 154, 1
Boella, G., Butler, R. C., Perola, G. C., Piro, L., Scarsi, L., & Bleeker, J. A. M. 1997, A&AS, 122, 299
Cagnoni, I., Papadakis, I. E., & Fruscione, A. 2001, ApJ, 546, 886
Chadwick, P. M., et al. 1999, ApJ, 513, 161
Chiaberge, M., & Ghisellini, G. 1999, MNRAS, 306, 551
Chiappetti, L., et al. 1999, ApJ, 521, 552
Dermer, C. D., & Chiang, J. 1998, NewA, 3, 157
Drury, L. O'C. 1983, Rep. Prog. Phys., 46, 973
Edelson, R. A., Griffiths, G., Markowitz, A., Sembay, S., Turner, M. J. L., & Warwick, R. 2001, ApJ, 554, 274
Edelson, R. A., & Krolik, J. H. 1988, ApJ, 333, 646
Edelson, R. A., et al. 1995, ApJ, 438, 120
Falomo, R., Pesce, J. E., & Treves, A. 1993, ApJ, 411, L63
Fiore, F., Guainazzi, M., & Grandi, P. 1999, Cookbook for *BeppoSAX* NFI Spectral Analysis (Rome: SDC)
Fossati, G., Maraschi, L., Celotti, A., Comastri, A., & Ghisellini, G. 1998, MNRAS, 299, 433
Fossati, G., et al. 2000a, ApJ, 541, 153
———. 2000b, ApJ, 541, 166
Ghisellini, G. 2001, in ASP Conf. Ser. 227, Blazar Demographics and Physics, ed. P. Padovani & C. M. Urry (San Francisco: ASP), 85
Ghisellini, G., Celotti, A., Fossati, G., Maraschi, L., & Comastri, A. 1998, MNRAS, 301, 451
Giommi, P., et al. 1998, A&A, 333, L5
Granot, J., & Königl, A. 2001, ApJ, 560, 145
Hartman, R. C., et al. 1999, ApJS, 123, 79
Hayashida, K., Miyamoto, S., Kitamoto, S., Negoro, H., & Inoue, H. 1998, ApJ, 500, 642
Hufnagel, B. R., & Bregman, J. N. 1992, ApJ, 386, 473
Kataoka, J., Takahashi, T., Makino, F., Inoue, S., Madejski, G. M., Tashiro, M., Urry, C. M., & Kubo, H. 2000, ApJ, 528, 243
Kataoka, J., et al. 2001, ApJ, 560, 659
Kino, M., Takahara, F., & Kusunose, M. 2002, ApJ, 564, 97
Kirk, J., Rieger, F., & Mastichiadis, A. 1998, A&A, 333, 452
Kusunose, M., Takahara, F., & Li, H. 2000, ApJ, 536, 299
Lawson, A. J., McHardy, I. M., & Marscher, A. 1999, MNRAS, 306, 247
Lockman, F. J., & Savage, B. D. 1995, ApJS, 97, 1
Maoz, D., & Netzer, H. 1989, MNRAS, 236, 21
Maraschi, L., et al. 1999, ApJ, 526, L81
Marshall, H. L., Urry, C. M., Sambruna, R. M., & Pesce, J. E. 2001, ApJ, 549, 938
Nandra, K., & Papadakis, I. E. 2001, ApJ, 554, 710
Nowak, M. A., Vaughn, B. A., Wilms, J., Dove, J. B., & Begelman, M. C. 1999, ApJ, 510, 874
Paltani, S. 1999, in ASP Conf. Ser. 159, BL Lac Phenomenon, ed. L. O. Takalo (San Francisco: ASP), 293
Paltani, S., Courvoisier, T. J.-L., Blecha, A., & Bratschi, P. 1997, A&A, 327, 539
Peterson, B. M., Wanders, I., Horne, K., Collier, S., Alexander, T., Kaspi, S., & Maoz, D. 1998, PASP, 110, 660
Pian, E., et al. 1997, ApJ, 486, 784
———. 1998, ApJ, 492, L17
Rees, M. J. 1978, MNRAS, 184, 61P
Rybicki, G. B., & Lightman, A. P. 1979, Radiative Processes in Astrophysics (New York: Wiley)
Sari, R., Piran, T., & Narayan, R. 1998, ApJ, 497, L17
Sembay, S., Warwick, R. S., Urry, C. M., Sokoloski, J., George, I. M., Makino, F., Ohashi, T., & Tashiro, M. 1993, ApJ, 404, 112
Sembay, S., Edelson, R., Markowitz, A., Griffths, R. G., & Turner, M. J. L. 2002, ApJ, in press
Sikora, M., Blazejowski, M., Begelman, M. C., & Moderski, R. 2001, ApJ, 554, 1
Simonetti, J. H., Cordes, J. M., & Heeschen, D. S. 1985, ApJ, 296, 46
Spada, M., Ghisellini, S., Lazatti, D., & Celotti, A. 2001, MNRAS, 325, 1559
Tagliaferri, G., Stella, L., Maraschi, L., Treves, A., & Celotti, A. 1991, ApJ, 380, 78
Takahashi, T., et al. 2000, ApJ, 542, L105
———. 1996, ApJ, 470, L89
Tanihata, C., Urry, C. M., Takahashi, T., Kataoka, J., Wagner, S. J., Madejski, G. M., Tashiro, M., & Kouda, M. 2001, ApJ, 563, 569
Tavecchio, F., et al. 2001, ApJ, 554, 725
Tavecchio, F., Maraschi, L., & Ghisellini, G. 1998, ApJ, 509, 608
Treves, A., et al. 1989, ApJ, 341, 733
Turner, T. J., George, I. M., Nandra, K., & Turcan, D. 1999, ApJ, 524, 667
Urry, C. M., et al. 1997, ApJ, 486, 799
Vermeulen, R. C., & Cohen, M. H. 1994, ApJ, 430, 467
Vestrand, W. T., Stacy, J. G., & Sreekumar, P. 1995, ApJ, 454, L93
Xie, G. Z., Li, K. H., Bai, J. M., Dai, B. Z., Liu, W. W., Zhang, X., & Xing, S. Y. 2001, ApJ, 548, 200
Zhang, Y. H. 2000, Ph.D. thesis, SISSA, Trieste
———. 2002, MNRAS, submitted
Zhang, Y. H., et al. 1999, ApJ, 527, 719
Zhang, Y. H., & Xie, G. Z. 1996, A&AS, 116, 289